Atmospheric Research 344 (2027) 109331

Contents lists available at ScienceDirect

Atmospheric Research

journal homepage: www.elsevier.com/locate/atmosres

Research paper

Mesoscale environments of tornadoes in Chile and along the U.S. west coast

Julio C. Marín [a,b,*], Bradford S. Barrett [c], Felipe Gutiérrez Cotapos [a], Diana Pozo [a,b]

[a] Department of Meteorology, Universidad de Valparaiso, Av. Gran Bretaña 644, Valparaiso, Chile
[b] Centro de Estudios Atmosféricos y Cambio Climático (CEACC), Universidad de Valparaiso, Valparaiso, Chile
[c] Independent Scholar, Raleigh, 27610, NC, United States

ARTICLE INFO

Keywords:
Chile
U.S. west coast
Tornadoes
Mesoscale environment

ABSTRACT

Despite a surge of interest following the May 2019 outbreak, many mesoscale details of tornadic environments in Chile remain unknown. In this study, we extend our understanding of tornadic environments in Chile and update our knowledge of environments during tornadoes along the U.S. west coast. To do so, the convective available potential energy derived from the most unstable parcel (MUCAPE), the effective bulk wind shear using the most unstable parcel (EBSMU), the storm-relative helicity in the 0–500-m layer (SRH500m), and two composite parameters, the Severe Hazards in Environments with Reduced Buoyancy (using wind shear over the effective inflow layer, SHERBE) and the Significant Tornado Parameter (STP), were analyzed during tornadoes from 1980–2023. Tornadoes in Chile tend to form in environments with lower MUCAPE than those along the U.S. west coast. However, EBSMU, SRH500m, SHERBE, and STP tend to be larger during tornadoes in Chile. This results in 50% of tornadoes in Chile, but only 25%–38% of tornadoes along the U.S. west coast, forming in high-shear, low CAPE (HSLC) environments. A cool, saturated boundary layer, low-level moisture fluxes, low cloud bases, and curved hodographs characterize the tornadic environments in all regions. Lightning activity is observed in at least 65% of tornadic storms in each region, but the largest flash density occurs during tornadoes in northern California. These results represent a significant advance in our understanding of the mesoscale conditions during tornadoes in Chile and along the U.S. west coast.

1. Introduction

There is new awareness among both the public and the scientific community of the threats posed by tornadic storms in central and south-central Chile, areas previously thought not to experience tornadoes (Vicencio et al., 2021). The purpose of this study is to extend our understanding of the mesoscale environments in which tornadoes occur in Chile and to compare them to environments during tornadoes along the U.S. west coast, which is a regional Köppen–Geiger climate analog to Chile (Kottek et al., 2006; Deitch et al., 2017) where tornadoes have been studied for several decades (Blier and Batten, 1994).

Much of our understanding of tornadoes in Chile comes from recent observational and modeling work motivated by the tornado outbreak of 30–31 May 2019, which was the most prolific in the country's history (Barrett et al., 2020; Marín et al., 2021; Vicencio et al., 2021). That two-day event featured seven documented tornadoes of intensities ranging from EF-0 to EF-2 (Aránguiz et al., 2020) and occurred during the passage and subsequent cyclonic breaking of a Rossby wave along 40°S, accompanied by a blocking high pressure anchored at 60°S (Vicencio et al., 2021). The tornadic storms developed in an unstable thermodynamic environment resulting from the poleward advection of modestly high equivalent potential temperatures in the lower troposphere. This environment was located to the east and south of an area of surface low pressure (Barrett et al., 2020) and beneath relatively cold polar air aloft associated with the wave break and subsequent quick eastward passage of multiple shortwave troughs (Vicencio et al., 2021). In this setting, weak levels of convective available potential energy (CAPE) combined with substantial amounts of low-level and deep-layer wind shear to comprise an environment commonly classified as "high-shear, low-CAPE" (HSLC) (Sherburn and Parker, 2014).

The HSLC environment, while often more challenging to predict than the high-CAPE environments (Dean and Schneider, 2008; Anderson-Frey et al., 2016) common to the U.S. Great Plains, southern Europe, southeast Asia, and subtropical South America (Schumacher et al., 2021; Tuckman and Emanuel, 2024), supports the formation of severe storms, including tornadoes (Sherburn et al., 2016), and poses more danger to the often-unaware public (Ashley et al., 2008). Analyses of surface observations, geostationary satellite imagery, and output from mesoscale simulations indicate that the tornadoes of May 2019 likely formed from supercell storms (Barrett et al., 2020). Vertical motions in supercell storms in HSLC environments result

* Corresponding author at: Department of Meteorology, Universidad de Valparaiso, Av. Gran Bretaña 644, Valparaiso, Chile.
E-mail address: julio.marin@meteo.uv.cl (J.C. Marín).

https://doi.org/10.1016/j.atmosres.2026.109331
Received 6 May 2026; Received in revised form 11 August 2026; Accepted 8 September 2026
Available online 14 September 2026

predominantly from perturbation pressure gradients associated with intense low-level mesocyclones (Wade and Parker, 2021) that develop in the strong vertical wind shear (Markowski and Richardson, 2009). High-resolution numerical experiments showed that in the 30–31 May 2019 event, the Andes topography blocked the synoptic-scale westerly flow below about 600 hPa, resulting in accelerated southward low-level jets adjacent to the higher terrain that enlarged low-level hodographs and enhanced vertical wind shear (Marín et al., 2021), thus supporting the formation and intensification of tornado-producing mesocyclones. Those numerical experiments also confirmed the modest contribution to storm buoyancy from the southeast Pacific Ocean, with a 2 K increase in offshore sea-surface temperatures yielding a 200–400 J kg^{-1} increase in onshore CAPE. Despite this detailed analysis, the mesoscale conditions typical of tornado environments in Chile remain unclear, including the extent to which they can be characterized as HSLC.

Tornadoes in Chile have occurred throughout the year but are most frequent in the cool season from May to August (Marín et al., 2024; Caballero-Morán and Rondanelli, 2025). Cool-season tornadoes have been documented in other global regions, including Brazil (de Lima Nascimento et al., 2014; Lopes and Nascimento, 2024), Japan (Inoue et al., 2011), England and Ireland (Clark, 2009; Tyrrell, 2007), Australia (Kounkou et al., 2009; Allen et al., 2021), western Europe (Avolio and Miglietta, 2023; Jiménez-Cavero, 2025; Lacroix et al., 2026b), and the southeastern U.S. (Childs et al., 2018; Anderson-Frey et al., 2019; Hua and Anderson-Frey, 2023; Campbell et al., 2024; Chalmers and Parker, 2026), typically forming in environments with high amounts of low-level wind shear and meager atmospheric instability, sometimes with most-unstable CAPE (MUCAPE) less than 500 J kg^{-1}. About 60% of the reported tornadoes in Chile have occurred in a relatively narrow latitudinal band from about 36°–40°S, although favorable conditions extend over a broader region. Convective parameters in the central and south-central parts of Chile (hereafter referred to more succinctly as "south-central Chile") show strong seasonality. Both the Severe Hazards in Environments with Reduced Buoyancy parameter, calculated using wind shear over the effective inflow layer, (SHERBE, Sherburn and Parker, 2014) and the Significant Tornado Parameter (STP, Thompson et al., 2004a, 2012) are largest there between May and August and smaller in other months (Marín et al., 2024). Values of CAPE and storm-relative helicity from 0–500 m (SRH500m) are also greatest in Chile in the late austral fall and winter months. Moreover, peak values of other parameters physically linked to tornado formation, including the vorticity generation parameter (VGP, Rasmussen and Blanchard, 1998), deep-layer bulk shear, and mean lower tropospheric relative humidity, are observed there between May and August (Caballero-Morán and Rondanelli, 2025).

Similar to Chile, tornadoes along the U.S. west coast, from California north to Washington, to the west of the Santa Ana, Peninsular, Transverse, Sierra, and Cascade mountain ranges, also occur most frequently in the cool season months (Monteverdi and Quadros, 1994), typically associated on the synoptic scale with the passage of tropospheric Rossby waves (Monteverdi et al., 2003). They tend to be weak ([E]F-2 or less) and short-lived (Blier and Batten, 1994; Miller and Mogil, 2011), hard to detect (Guyer and Dean, 2010), and sometimes feature little lightning activity (McAvoy et al., 2000) due to limited instability in the mixed-phase region of the cloud (Van Den Broeke et al., 2005). On the mesoscale, tornadoes along the U.S. west coast tend to form in environments with modest CAPE and large values of both low-level and deep-layer wind shear (Braun and Monteverdi, 1991; Monteverdi and Quadros, 1994; Blier and Batten, 1994; Monteverdi et al., 2001). In these conditions, the magnitude of shear (and not necessarily of CAPE) can sometimes serve as a discriminator of tornadic storms, with greater shear values favoring tornado environments (Monteverdi et al., 2003). Understanding the spatial and temporal variability of several key convective parameters during tornado events in Chile and how they compare to the U.S. west coast is a key goal of this study.

Even with the case studies on the May 2019 outbreak and the climatologies of Marín et al. (2024) and Caballero-Morán and Rondanelli (2025), many details of tornado environments in Chile remain unknown. These uncertainties include the seasonal and spatial variability of mesoscale environments during tornadoes in Chile and how these mesoscale conditions evolve temporally in the hours before tornado events. Details on possible lightning activity during tornadoes in Chile are also unknown and, to the authors' knowledge, have never been studied before. The purpose of this study is to partially fill those gaps. We do so by analyzing the mesoscale environments during tornadoes reported in Chile over the past 44 years, from 1980–2023. We then contextualize the tornado environments by comparing and contrasting them with the mesoscale conditions present during tornadoes reported along the U.S. west coast over the same period. Despite having been studied for longer, many details of U.S. west coast tornado environments also remain unclear, and the limited number of studies that have comprehensively examined those details, including work by Monteverdi and Quadros (1994), Blier and Batten (1994), Lipari and Monteverdi (2000), Monteverdi et al. (2001), Hanstrum et al. (2002) and Monteverdi et al. (2003), are now more than 20 years old. Therefore, alongside gaining new knowledge of the mesoscale environments during tornadoes in Chile, a parallel goal of this study is to update our understanding of such environments during tornadoes along the U.S. west coast. The remainder of this article is organized as follows: data and methods are presented in Section 2, results are presented in Section 3, and conclusions and discussion are presented in Section 4.

2. Data and methodology

2.1. Study regions and tornado reports

Locations, dates, and times of the tornadoes in Chile analyzed in this study (Fig. 1a) were taken from a recently created database of tornado and waterspout activity (Bastías-Curivil et al., 2024). That database, which was developed from a collaboration between the Meteorological Service of the Chilean Navy (SERVIMET), the Chilean Meteorological Directorate (DMC), researchers at the University of Chile, and dedicated hobbyists (Vicencio et al., 2021), forms part of a broader tornado record for South America (Salio et al., 2024). It includes reports dating back to the 16th century, although 95% of the tornado reports in the database come from the most recent two decades, and 82.5% are from just the last ten years (2014–2023). This recency bias is likely explained by the increasing availability of mobile recording devices, greater public awareness of tornado activity, and demographic expansion in the previously more sparsely populated areas of south-central Chile (Marín et al., 2024; Caballero-Morán and Rondanelli, 2025). Teams from the DMC, SERVIMET, and the University of Chile began routine surveys of tornado damage via near-real-time, in-person assessments starting approximately in 2019. For earlier tornado reports, they retroactively determined the dates, locations, and estimated intensities using available chronicles, newspaper articles, social and other media photos and videos, the scientific literature, and books (D. Campos, personal communication, 2026). For each tornado report, the database includes summaries of damage surveys and links to media, where available, as well as an estimate of the intensity according to the Enhanced Fujita (EF) damage scale. The estimated intensities range from EF-0 to EF-3, but because tornado intensity ratings in Chile have not yet been systematically evaluated, they are not considered further in this study. More details on the Chilean tornado database are available from Bastías-Curivil et al. (2024). From 1980–2023, we identified 40 tornadoes in Chile, although we believe this number is likely an under count of the actual tornado activity due to the biases mentioned earlier and complicated by the absence of routine weather surveillance radar in Chile (Rojas et al., 2021).

Locations, dates, and times of the tornadoes along the U.S. west coast analyzed in this study (Fig. 1b) were taken from the National

Weather Service (NWS) Storm Data maintained by the NOAA/NWS Storm Prediction Center, available at http://www.spc.noaa.gov/wcm/#data. That database contains information on tornadoes in the U.S. dating from 1950 (Maas et al., 2024) and has known strengths and weaknesses (Edwards et al., 2022), including a bias towards tornado reports in populated areas (Doswell et al., 1999). In this study, we focus on tornadoes along the U.S. west coast in three domains located upstream of major mountain ranges: Washington–Oregon (WaOr), Northern California (NoCa), and Southern California (SoCa) (Fig. 1b). From 1980–2023, we identified 102 tornadoes in Washington–Oregon, 229 tornadoes in northern California, and 100 tornadoes in southern California, and intensities range from [E]F-0 to [E]F-2. Differences between the hours of tornado reports in each region were tested for statistical significance using a two-sample Kolmogorov–Smirnov test, with the null hypothesis explaining that the data in each region are from the same continuous distribution.

Unlike in Chile, where the Andes mountains extend in approximately a north–south line that is both parallel to, and an average of 150 km from, the coast in the study region, the orientation of the topography in the three U.S. regions is more varied (Fig. 1b). In WaOr, the Cascade mountains are oriented approximately south-southwest to north-northeast and are between 150–250 km from the coast. In NoCa, the Coast ranges and Sierra mountains are both oriented in a northwest–southeast line and located an average of 80 km and 300 km from the Pacific coast, respectively. The California Central Valley is located between these two ranges. While some tornado reports are interspersed among the Coast ranges, approximately 85% of them are located in the Central Valley, meaning that, on average, most tornado reports in NoCa are located farther from the Pacific Ocean than in the other regions. In the more compact SoCa region, which extends less than 250 km spatially compared with more than 400 km for both NoCa and WaOr and 1200 km for Chile, the Transverse range forms the northern boundary of the region. It aligns along a west-northwest to east-southeast axis, while the Peninsular range and Santa Ana mountains form the eastern boundary of the region and align along an approximately north–south axis. Both groups of mountain ranges in SoCa are located less than 100 km from the coast, meaning that tornado reports in SoCa are relatively closer to the Pacific Ocean than reports in the other U.S. regions and more tightly clustered in the populated areas of the region.

2.2. Atmospheric data

We used the fifth-generation reanalysis of the European Centre for Medium-Range Weather Forecasts (ECMWF) (ERA5, Hersbach et al., 2020) to assess the mesoscale convective environments during tornadoes in Chile and along the U.S. west coast. The ERA5 data were analyzed from 1980–2023 at hourly temporal resolution, 0.25° × 0.25° horizontal resolution, and over 24 pressure levels from the surface to 100 hPa. The ERA5 reanalysis has been used to analyze the mesoscale convective environments in recent studies of tornadoes in the United States (Taszarek et al., 2021a,b; Gensini et al., 2021; Pilguj et al., 2022; Tippett et al., 2024; Kiefer et al., 2026) and other parts of the world (Taszarek et al., 2021b; Shikhov et al., 2022; Pilorz et al., 2024; Veloso-Aguila et al., 2024; León-Cruz, 2025; Zhang et al., 2025), including Chile (Marín et al., 2024; Caballero-Morán and Rondanelli, 2025).

Potential relationships between lightning and tornadoes in HSLC environments remain understudied and thus largely unknown. There is some indication that tornadic storms in these environments exhibit a "jump" in lightning flash activity prior to tornadogenesis (McAvoy et al., 2000; Clark, 2009), similar to tornadoes in high-CAPE environments (Bridenstine et al., 2005; Schultz et al., 2009; Yu et al., 2025). However, those results are based mostly on studies of individual cases using ground-based instrumentation, thus limiting comparability with lightning measurements from this study. To explore lightning activity during tornadoes in Chile and along the U.S. west coast, we examined data from the Geostationary Lightning Mapper (GLM) L2 product. The GLM instrument was included on the payload of the Geostationary Operational Environmental Satellite R series (GOES-R), the first of which became operational in 2017 (Schmit et al., 2017). The GLM is a near-infrared optical transient detector that measures total lightning (in-cloud, cloud-to-cloud, and cloud-to-ground) between 52°N–52°S at approximately 10-km horizontal resolution with 70%–90% day and night flash detection (Goodman et al., 2013). The GLM instrument detects a greater fraction of lightning in the tropics than at higher latitudes; however, the effects of detection variability are not considered here. The GLM lightning data were available for 23 tornadoes in Chile between July 2017–December 2023, and 19 (82.6%) of them were found to have lightning activity within 2° × 2° spatially and one hour of the tornado report. In WaOr, 11 (64.7%) of the 17 tornadoes occurring in the GLM observational period had lightning activity, while lightning activity was found in 17 (68.0%) of the 25 tornadoes in NoCa and 5 (100%) of the 5 tornadoes in SoCa. Flash latitude and longitude were downloaded from https://www.earthdata.nasa.gov.

2.3. Convective parameters

We extracted vertical profiles of geopotential, air temperature, relative humidity, and u and v wind components from the ERA5 reanalysis and used them to calculate convective parameters commonly employed to diagnose tornado environments. Since the ERA5 does not explicitly provide dew point temperature on pressure levels, we calculated it following Romps (2021). We calculated each convective parameter using the R package thundeR (Taszarek et al., 2021b), which is available from https://bczernecki.github.io/thundeR/. We analyzed the CAPE derived from the most unstable parcel (MUCAPE), the effective bulk wind shear using the most unstable parcel (EBSMU) (Thompson et al., 2004b), and the SRH in the 0–500-m layer (SRH500m) using the left-moving Bunkers storm motion for Chile and the right-moving Bunkers storm motion for the U.S. In addition, we analyzed two composite parameters, SHERBE and STP. Differences between each parameter in each region were tested for statistical significance using a two-sample Kolmogorov–Smirnov test, with the null hypothesis explaining that the parameters in each region are from the same continuous distribution. Differences in mean values of each parameter in each region were also evaluated for statistical significance using a Student's t test.

We calculated the Severe Hazards in Environments with Reduced Buoyancy (SHERB) parameter, which was developed by Sherburn and Parker (2014) to characterize the severe weather potential, including tornadoes, from storms that form in HSLC conditions. This parameter can be calculated using fixed- or variable-layer wind shear, and in this study, we used the SHERBE parameter, which employs the variable-layer EBSMU as described in Sherburn and Parker (2014). The SHERBE parameter was the most skillful of the 16 convective parameters tested by Sherburn et al. (2016) at discriminating tornadic storms from nontornadic ones in HSLC conditions. We adopt their definition of an HSLC environment as one with MUCAPE < 1000 J kg^{-1} and EBSMU > 18 m s^{-1}, and SHERBE values above 1 are most commonly associated with severe weather.

To further investigate potentially tornadic convective environments, we calculated the STP, which is a widely used composite convective parameter that skillfully discriminates between significant and nontornadic environments in supercell thunderstorms whose motions deviate from the mean deep-layer shear vector (Thompson et al., 2003). In this study, we calculated the effective-layer version based on SRH500m, following Coffer et al. (2019). The STP has historically been used to differentiate environments supporting either weak (EF-0 and EF-1) tornadoes or none at all from those in which significant (EF-2+) tornadoes occur, such as in the U.S. east of the Rocky Mountains (Grams et al., 2012; Brotzge et al., 2013; Gensini and Brooks, 2018; Strader et al., 2024), East Asia (Zhou et al., 2022; Zhang et al., 2025), and the La Plata basin in South America (Veloso-Aguila et al., 2024). Although

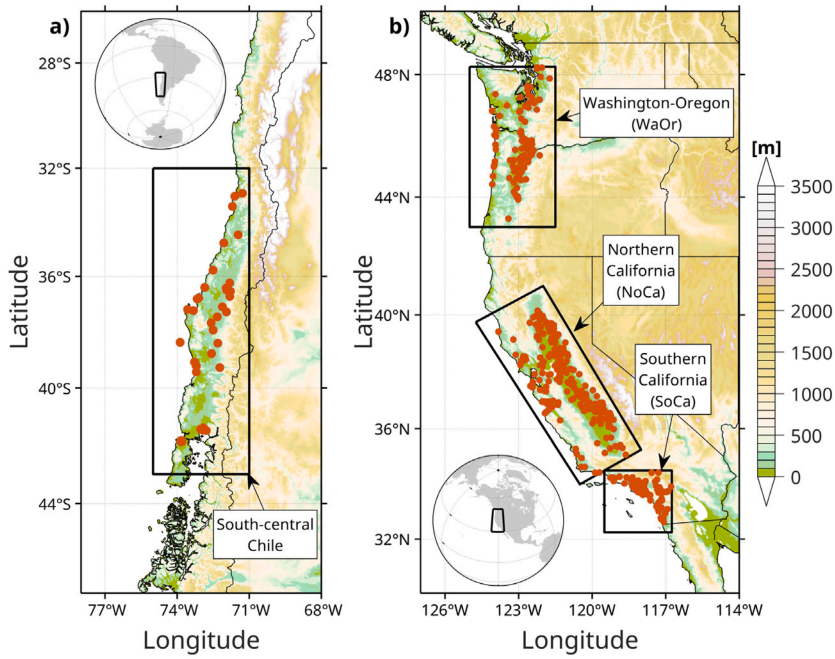

Fig. 1. The four domains analyzed in this study and the locations of tornado reports in (a) Chile and (b) the western U.S. between 1980 and 2023. Terrain elevation (m) is shaded.

Table 1
Convective parameters analyzed in this study.

Abbreviation	Name	Units
MUCAPE	CAPE derived from the most-unstable parcel	J kg^{-1}
EBSMU	Bulk wind shear from the most unstable parcel level upward to 40%–60% of the equilibrium level height	m s^{-1}
SRH500m	Storm-relative helicity for the 0–500-m layer, calculated using the left-moving Bunkers storm motion for Chile and the right-moving storm motion along the U.S. west coast	m^2 s^{-2}
SHERBE	Severe hazards in environments with reduced buoyancy (SHERB) parameter using effective shear (Sherburn and Parker, 2014)	dimensionless
STP	Significant tornado parameter, following Coffer et al. (2019)	dimensionless

Taszarek et al. (2020) concluded that the STP was not an effective parameter for tornado prediction in Europe because it was originally calibrated for the large-CAPE environment in the U.S., many different variants of STP have been proposed (Thompson et al., 2012), and some of those versions have been found to skillfully identify tornado environments of all intensities (Zhang et al., 2025). Indeed, Marín et al. (2024) recently showed that the STP can effectively discriminate the location, timing, and seasonality of all tornado environments in Chile, not just those supporting EF-2+ intensities, despite the relatively low CAPE values of those environments. Therefore, we have chosen to include analyses of STP to aid in comparing and contrasting tornado environments in Chile with those along the west coast of the United States. Similar to SRH500m, the STP calculation in this study is based on a left-moving storm for Chile and a right-moving storm for the U.S. west coast. Following Thompson et al. (2003), we set STP to zero when EBSMU < 12.5 m s^{-1} in Chile and < 7.5 m s^{-1} for the U.S. west coast (a lower threshold since many tornadoes there form when EBSMU is below 12.5 m s^{-1}). It is worth noting that the values of STP seen during tornadoes in Chile and along the U.S. west coast are typically between 0–0.3, which is smaller than the threshold of STP ≥ 1 suggested by Thompson et al. (2003) to discriminate between significantly tornadic and nontornadic storms. These lower values are primarily due to the lesser CAPE values seen during the tornadoes in this study. A summary description of the convective parameters analyzed in this study is given in Table 1.

3. Results

3.1. Diurnal, seasonal, and interannual variability

On the diurnal time scale, tornadoes in both Chile and along the U.S. west coast tend to occur most frequently between 1000 and 1800 local time (LT) and least frequently between 2000 and 0500 LT (Fig. 2a). The most frequent hour of tornado occurrence in Chile is 1500 LT, whereas it is 1400 LT in WaOr and NoCa, and it is 1200 LT in SoCa. This diurnal variability is in good agreement with Blier and Batten (1994), who noted an afternoon peak in tornado frequency in both NoCa and SoCa, with the peak in SoCa occurring a few hours earlier than in NoCa. The hours when tornadoes occur in Chile, WaOr, and NoCa are statistically indistinguishable from one another at the 95th percentile. However, tornadoes in SoCa occur earlier than in the other two U.S. west coast regions, a difference that is statistically significant at the 95th percentile.

The diurnal maximum in tornado frequency in all regions occurs during the hours of greatest surface insolation and heating, and the diurnal minimum occurs overnight during nocturnal surface cooling. This diurnal alignment suggests that lower tropospheric vertical accelerations driven by insolation (Markowski and Richardson, 2013; Davies-Jones, 2015), although weak in the autumn and winter months, are nevertheless important to tornado activity in all regions during those months. It also suggests that the onset of early-evening boundary-layer decoupling and the concurrent strengthening of the low-level

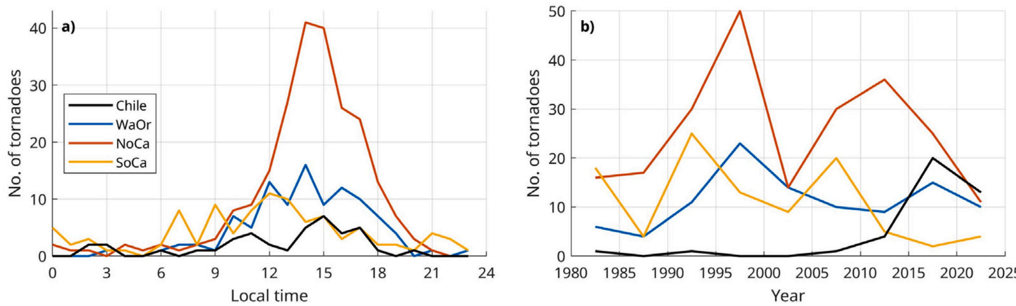

Fig. 2. Total number of tornado occurrences by (a) hour and by (b) year (5-year interval) in Chile (black line), WaOr (blue line), NoCa (red line) and SoCa (yellow line).

shear vector (Coffer and Parker, 2015) is not necessary to generate the low-level vertical vorticity necessary for tornadogenesis (e.g., King et al., 2017; Sherburn et al., 2019) in either Chile or along the U.S. west coast. This diurnal pattern differs meaningfully from other tornado-prone regions, particularly the U.S. Great Plains, where the springtime maximum in tornado frequency is temporally out of phase with the insolation maximum by several hours. There, the time lag allows the hours with large to extreme values of CAPE to overlap temporally with diurnally increasing low-level shear profiles and lowering lifting condensation levels (Davies and Johns, 1993; Johns et al., 1993; Rasmussen and Blanchard, 1998; Rasmussen, 2003; Kis and Straka, 2010). That parameter space juxtaposition (Clark, 2017) often becomes very favorable for tornadogenesis during the boundary-layer decoupling that begins a few hours prior to local sunset (Anderson-Frey et al., 2016; Brown et al., 2021; Sabol and Nowotarski, 2025).

On the seasonal time scale, tornadoes in Chile are most likely to develop in late fall and winter months, with the largest fraction of tornadoes (25%–35%) found in May and June (Fig. 3a). Normalized MUCAPE averaged over south-central Chile (Fig. 1a) peaks in austral summer but shows a clear secondary maximum in austral fall and winter, specifically in May and June (Fig. 3a). Normalized values of the other analyzed convective parameters (EBSMU, SRH500m, SHERBE, and STP) averaged over south-central Chile also peak in May and June, highlighting the favorable environmental conditions concurrent with the peak in tornado likelihood in Chile during those two months. This seasonality of the kinematic parameters associated with tornadoes is in good agreement with Marín et al. (2024) and Caballero-Morán and Rondanelli (2025), who noted peaks in those parameters in May and June in south-central Chile. The seasonality in both tornado frequency and the kinematic parameters also aligns with the climatological maxima in precipitable water and precipitation (Barrett et al., 2011; Barrett and Hameed, 2017; Pozo et al., 2023), extratropical storm activity (Barrett et al., 2009), landfalling atmospheric rivers (Viale et al., 2018; Campos and Rondanelli, 2023), and horizontal moisture fluxes (Valenzuela and Garreaud, 2019) in Chile. However, a detailed analysis of the synoptic-scale processes common to tornadoes in Chile remains absent from the literature.

Tornadoes in WaOr are most likely to develop in two separate periods of the year. The largest fraction of tornadoes (17%–21%) occurs in the boreal autumn months of September–October, followed by a secondary maximum (16%) in early summer (June) (Fig. 3b). Tornadoes in WaOr are least likely to occur in July and August. The two maxima correlate well with the two peaks in convective storm activity in WaOr (Miller and Mogil, 2011). Additionally, the autumn maximum in tornado frequency corresponds with the annual peak in sea surface temperatures in the adjacent northeast Pacific Ocean (Legaard and Thomas, 2006) and the seasonal increase in extratropical storm activity in the Pacific Northwest region (Mass, 2021). Normalized values of EBSMU, SHERBE, and STP averaged over the WaOr domain (Fig. 1b) also show bimodal distributions, with maximum values in the boreal spring and fall months and minimum values in July (Fig. 3b). Normalized SRH500m in WaOr is a minimum in July and a maximum in boreal winter. It is important to note that none of the kinematic shear-based parameters (nor their composites) reach a maximum in WaOr during the June secondary peak in tornado frequency; only the thermodynamic parameter MUCAPE reaches a maximum in June. The opposite is seen during the October peak in tornado frequency: MUCAPE is lower while the kinematic parameters in WaOr are at or near their maximum seasonal values. This out-of-phase relationship between the kinematic and thermodynamic parameters in WaOr highlights the complex, coupled ways that processes captured by both sets of parameters contribute to tornadogenesis.

Tornadoes in NoCa are most frequent between December and April, with the largest fraction, 22%, in March (Fig. 3c). Tornadoes in SoCa are most frequent between November and March, with the largest fraction, 19%, in February (Fig. 3d). The likelihood of a tornado is lowest in both NoCa and SoCa in the boreal summer months. Normalized MUCAPE is largest in summer in NoCa and SoCa, during the minimum in tornado frequency, but a secondary maximum in MUCAPE appears in both regions from January to March. This secondary maximum in CAPE coincides with the months with the greatest frequency of tornadoes (Fig. 3c,d). In NoCa, the largest values of normalized EBSMU and SHERBE occur between February and April, and both SRH500m and STP peak in boreal winter (Fig. 3c), coinciding with the peak in tornado frequency in NoCa. In SoCa, the normalized values of EBSMU, SRH500m, SHERBE, and STP resemble a bimodal distribution with peaks in both the summer-fall months and between January and March. The peak between January–March in SoCa coincides with the months with the greatest frequency of tornadoes there (Fig. 3d). Similar to Chile, the peak in frequency of tornadoes in both NoCa and SoCa during the extended winter months aligns with the maxima in precipitation (Dong and Dai, 2015; Swain et al., 2015) and the frequency of extratropical cyclones (Hoskins and Valdes, 1990) in those months.

On the interannual time scale, the number of tornado reports in Chile has increased substantially in the last two decades, with nearly 55% of the reports from 1980–2023 coming in just the eight years since 2015 (Fig. 2b). However, as previously mentioned, this increase is likely associated with non-meteorological factors, complicating any potential analysis of interannual variability of tornadoes in Chile. Indeed, Marín et al. (2024) found that the number of favorable tornadic environments in south-central Chile showed no long-term trend between 1959 and 2021. Along the U.S. west coast, the number of tornado reports appears to have either decreased or not changed significantly over the last decade compared to the period from 1990 to 2010, in agreement with Guo et al. (2016) and Moore (2018). The reasons for this variability are unclear, and it is likely complicated by the relatively low number of tornadoes reported in a given year along the U.S. west coast. Most studies analyzing long-term trends in tornado activity in the U.S. tend to focus on regions with greater tornado frequency, such as the Great Plains, Midwest, and Southeast (Gensini and Brooks, 2018; Nouri et al., 2021). In the U.S. east of the Rocky Mountains, while the annual number of [E]F-1+ tornadoes has remained relatively

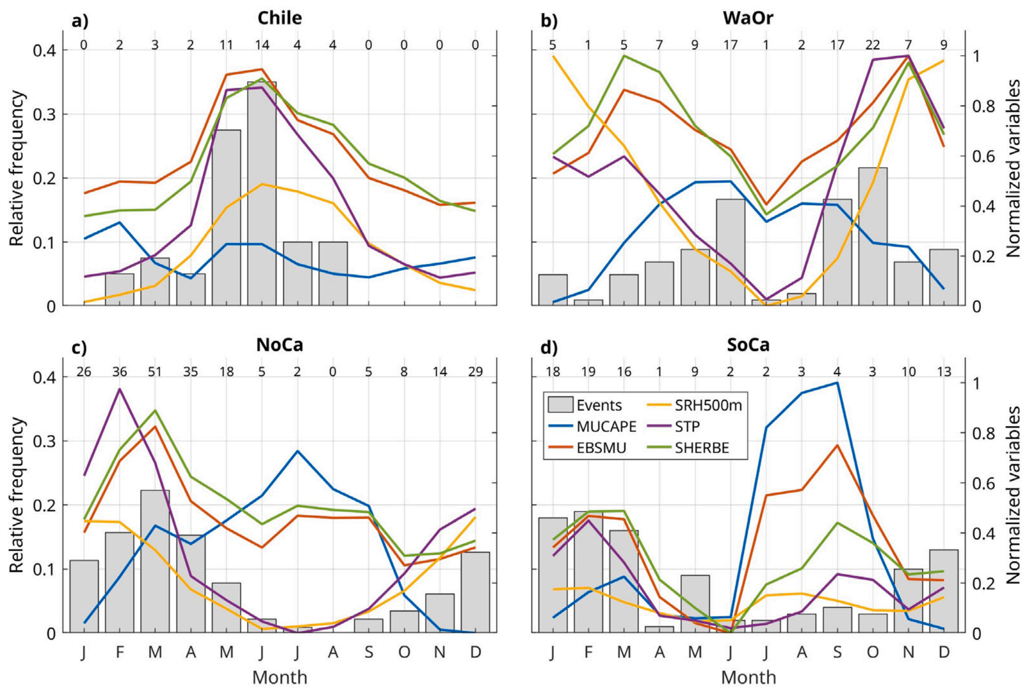

Fig. 3. Relative frequency of tornado reports by month, along with monthly normalized values of MUCAPE, EBSMU, SRH500m, SHERBE, and STP averaged over the domains of (a) Chile, (b) WaOr, (c) NoCa, and (d) SoCa. The number of tornadoes in each month in each region is given across the top of each panel.

steady (Brooks et al., 2014), statistically robust increases in tornado frequency have been documented in the Southeast alongside decreases in the Great Plains (Guo et al., 2016) that could be the result of either climate change or large-scale circulations, or both, projecting onto the climate system (Gensini and Brooks, 2018). In addition, the La Niña phase of the El Niño-Southern Oscillation (ENSO) has been found to increase tornado frequency in the southeast U.S. from January–April (Cook and Schaefer, 2008) by causing a pivot of the mean position of the polar jet stream northward into the central and northern U.S. that subsequently increases surface cyclone activity, CAPE, and vertical wind shear (Cook et al., 2017) to its south. In Europe, the number of annual reported tornadoes has seen a nearly ten-fold increase beginning in approximately 1995 (Groenemeijer and Kühne, 2014), a change attributed to non-meteorological reporting factors (Antonescu et al., 2017) similar to Chile. In addition, tornadoes in Europe are favored during the positive phase of the Atlantic Multidecadal Oscillation (AMO), the positive phase of the North Atlantic Oscillation (NAO) in winter, and the negative NAO in summer (Lacroix et al., 2026a) due to each oscillation modulating the mean extratropical storm track and associated instability and wind shear. It is thus plausible that large-scale atmospheric circulations, including ENSO, the Southern Annular Mode (SAM), the NAO, and the Pacific Decadal Oscillation (PDO), exert some influence on interannual and long-term tornado frequency in Chile and along the U.S. west coast, as each of these circulations projects onto Rossby wave and extratropical storm activity in both the Northeast and Southeast Pacific oceans across a range of time scales (Mo and Higgins, 1998; Dai and Wigley, 2000; Montecinos and Aceituno, 2003; Reboita et al., 2009; Mantua and Hare, 2002; Aceituno et al., 2020; Nouri et al., 2021). Indeed, multi-year tornado counts in WaOr, NoCa, and SoCa show some indications of interannual variability (Fig. 2b). However, that analysis is beyond the scope of this study.

3.2. Probability distributions of convective parameters during tornadoes

Probability distributions of the five convective parameters analyzed in this study show the range of variability of the mesoscale conditions associated with tornadoes in Chile and along the U.S. west coast. The distributions presented here were created using ERA5 reanalysis values from the nearest grid point and the three hours before and during each tornado report.

More than 95% of MUCAPE values during tornadoes in both Chile and along the U.S. west coast range from 0–1200 J kg^{-1} (Fig. 4a). The most common values of MUCAPE (in over 50% of the tornadoes in each region) are between 0–400 J kg^{-1}, underscoring the low-CAPE nature of the mesoscale environments. The distribution of MUCAPE during tornadoes in Chile is most similar to that during tornadoes in SoCa, while distributions of MUCAPE in WaOr and NoCa most resemble one another. Both the similarities and the differences in MUCAPE distributions among the regions are statistically significant at the 95th percentile. Lower values of MUCAPE (less than 400 J kg^{-1}) are more frequent during tornadoes in Chile and SoCa, whereas larger values of MUCAPE (greater than 600 J kg^{-1}) are more frequent during tornadoes in WaOr and NoCa. The values of MUCAPE during tornadoes in Chile and along the U.S. west coast are comparable to the weak tornado category of Púčik et al. (2015) for central Europe (median value near 300 J kg^{-1}) and the [E]F-0 and [E]F-1 tornadoes of Anderson-Frey et al. (2019) for the southeast U.S. (median values 450–500 J kg^{-1}).

The overall distribution of EBSMU during tornadoes in Chile is similar to the distributions of EBSMU during tornadoes across all three regions along the U.S. west coast (Fig. 4b). Bulk shear in more than 50% of tornadoes in both Chile and the U.S. west coast is between 7.5–17.5 m s^{-1}, and the maximum bulk shear values in all regions are around 30 m s^{-1}. These values compare very favorably to the typical values of 0–6 km bulk shear found during tornadic storms in Europe (14–15 m s^{-1}) (Brooks, 2009; Púčik et al., 2015; Taszarek et al., 2020) and Australia (15 m s^{-1}) (Allen and Karoly, 2014) and are slightly below the median value of bulk shear during tornadic storms in the U.S. east of the Rocky Mountains (18–20 m s^{-1}) (Rasmussen and Blanchard, 1998; Taszarek et al., 2020). However, some regional differences are observed in this study. For example, EBSMU values larger than 15 m s^{-1} are more frequent during tornadoes in Chile and less frequent during tornadoes along the U.S. west coast. The most frequent value of EBSMU during tornadoes along the U.S. west coast is between 12–14 m s^{-1}, whereas it is larger in Chile, between 16–18 m

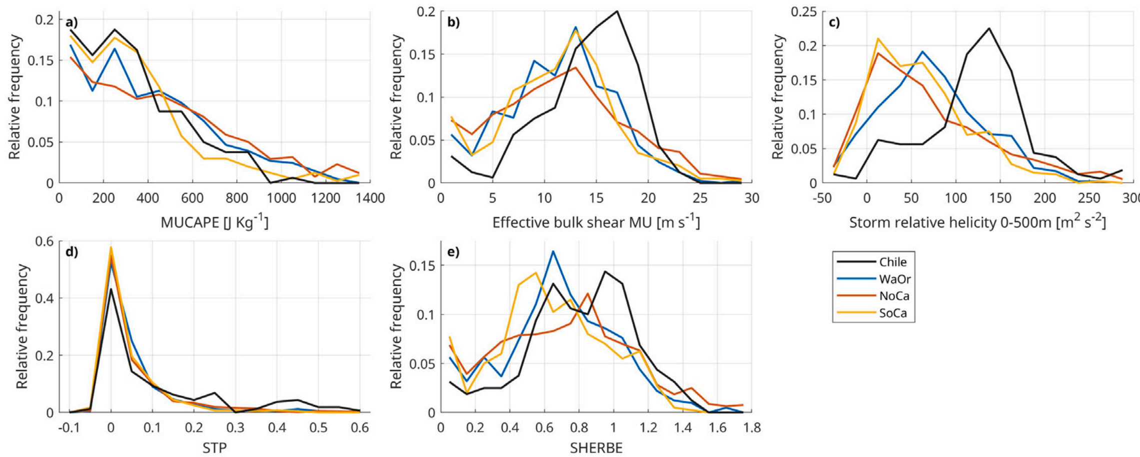

Fig. 4. Probability distributions of (a) MUCAPE, (b) EBSMU, (c) SRH500m, (d) SHERBE, and (e) STP at the nearest grid point and three hours prior to each tornado reported in Chile (black line), WaOr (blue line), NoCa (red line), and SoCa (yellow line). The SRH500m and STP values for Chile were multiplied by −1 for comparison purposes.

s^{-1}. These differences in EBSMU values between tornadoes in Chile and the three U.S. regions are statistically significant at the 95th percentile. However, during tornadoes in the U.S. west coast regions, values of EBSMU are not statistically significantly distinct from one another ($p > 0.124$). This statistical similarity across such a broad latitudinal band suggests that the three U.S. regions could share large-scale mechanisms responsible for their patterns in bulk shear. In the same way, the statistical separation between EBSMU during tornadoes in Chile and the U.S. west coast suggests that there could be mechanistic differences between topographical features and the large-scale patterns responsible for bulk shear in the two countries. Detailed and comparative analyses of these large-scale patterns during tornadoes in Chile and along the U.S. west coast are suggested for future study.

The distribution of SRH500m during tornadoes in Chile seems to be different from the three U.S. regions, with more than 50% of tornadoes in Chile having SRH500m between 50–150 m^2 s^{-2} (in magnitude, as SRH values in Chile in Fig. 4c are multiplied by −1 for ease of comparison). On the other hand, the distribution of SRH500m during tornadoes in NoCa is most similar to SoCa and, to a lesser extent, to WaOr. Despite these similarities, some important differences are observed. For example, the distribution of SRH500m during tornadoes in Chile is shifted more towards larger values than in any of the three regions of the U.S. west coast. The most frequent SRH500m values during tornadoes in both NoCa and SoCa are below 25 m^2 s^{-2} and between 50–75 m^2 s^{-2} in WaOr, while the most frequent values in Chile are between 125–150 m^2 s^{-2}. Values of SRH500m during tornadoes in all regions are statistically significantly different from one another at the 95th percentile. These differences suggest that each region could have unique mesoscale characteristics that are responsible for its patterns of SRH500m during tornadoes.

The magnitudes of SRH500m most common during tornadoes in Chile are similar to the median value of SRH500m (approximately 160 m^2 s^{-2}) that Lovell and Parker (2022) found for simulated tornadoes in cold-season HSLC environments in the U.S. mid-Mississippi valley. The tilting and vertical stretching of streamwise vorticity of this magnitude is more than sufficient to generate the low-level mesocyclones that often precede tornadogenesis (Markowski and Richardson, 2009; Schenkman et al., 2014; Fischer and Dahl, 2022; Fischer et al., 2024). The relatively lower magnitudes of SRH500m seen during tornadoes in the three regions along the U.S. west coast are similar to the SRH500m during weak tornadoes ([E]F-0 to [E]F-1) analyzed by Coffer et al. (2019) east of the Rocky Mountains. While smaller in magnitude than during tornadoes in Chile, low-level streamwise vorticity of this magnitude is still sufficient to support tornadogenesis (Thompson et al., 2007). It is also possible that either the low-level wind field or the prescribed storm motion, or both, are undersampled in the reanalysis (Coffer et al., 2025) and thus the magnitude of SRH500m is misrepresented in either Chile or along the U.S. west coast.

Between 42%–60% of STP values during tornadic environments in each region are zero (note that, as with SRH500m, STP in Chile is multiplied by −1 for ease of comparison). Nevertheless, non-zero values of STP appear to be more frequent during tornadoes in Chile than during tornadoes in any of the regions along the U.S. west coast. For example, STP values larger than 0.15 are most frequently observed in Chile. STP values during tornadoes in Chile are statistically significantly different from those in the three regions of the U.S. ($p < 0.01$). The distributions of STP in WaOr and NoCa are also statistically significantly different from one another ($p < 0.02$). This pattern is also seen in the other composite parameter, SHERBE. The most frequent SHERBE value in Chile is between 0.9–1.0, which is larger than in any of the regions along the U.S. west coast (Fig. 4e). The most frequent SHERBE value is between 0.8–0.9 in NoCa, which is slightly smaller than in Chile, and the distributions of SHERBE values during tornadoes in both SoCa and WaOr are shifted towards even smaller values (0.5–0.6 and 0.6–0.7, respectively). All the SHERBE distributions from the four regions are statistically significantly different from one another ($p < 0.003$).

Since values of the two shear parameters during tornadoes in Chile are statistically significantly greater than those during tornadoes in each of the three regions along the U.S. west coast, we next tested whether tornadic environments in Chile are more often characterized as HSLC. This analysis is somewhat complicated by the limited statistically significant differences in instability between Chile and the three U.S. regions. One solution to that challenge is to examine the thermodynamic and kinematic parameters together, similar to Brooks (2009). Relative distributions of MUCAPE versus EBSMU (Fig. 5a–c) and SRH500m (Fig. 5d–f) highlight the differences in the distributions of MUCAPE, EBSMU, and SRH500m between Chile and the three U.S. regions. In each instance, higher values of both bulk shear and storm-relative helicity in Chile tend to occur in lower CAPE environments. Similarly, higher values of CAPE during tornadoes along the U.S. west coast are more frequently found alongside lower values of bulk shear and helicity, especially in WaOr and NoCa (Fig. 5a–b,d–e). These differences are statistically significant ($p < 0.02$) using the non-parametric Kolmogorov–Smirnov and energy distance (Székely et al., 2013) tests. Not surprisingly, tornado environments in Chile are thus more often classified as HSLC than those along the U.S. west coast. Indeed, half of the tornadoes in Chile from 1980–2023 formed in HSLC environments, while only 25% to 38% of tornadoes along the U.S. west coast formed in HSLC conditions (Table 2).

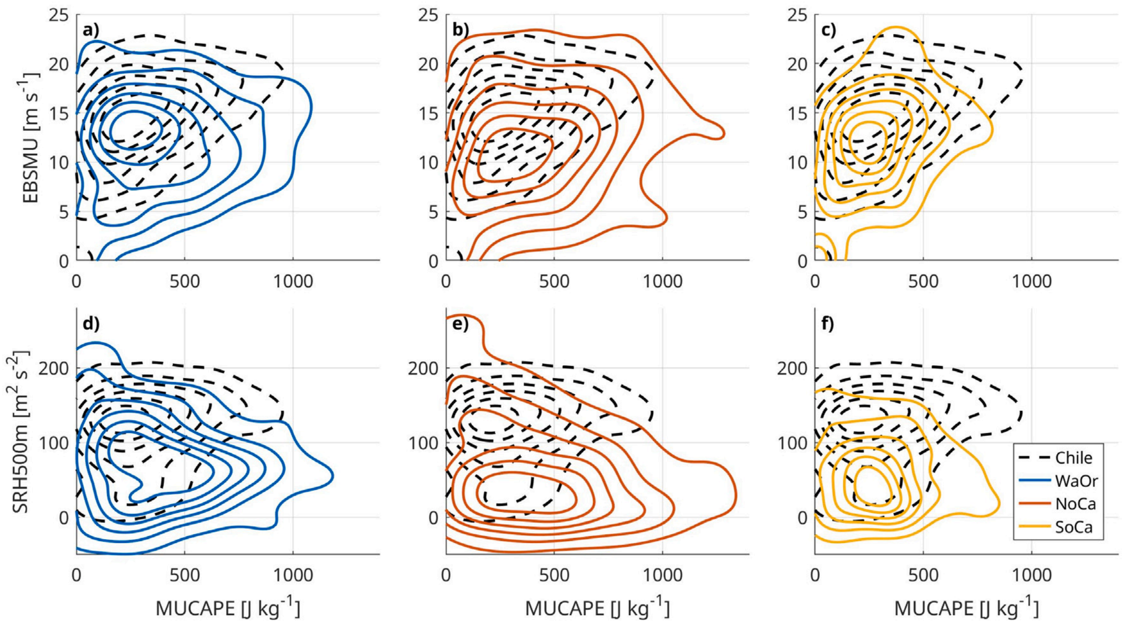

Fig. 5. (a)–(c) Relative distributions of MUCAPE versus EBSMU for Chile (dashed black line), WaOr (blue line), NoCa (red line), and SoCa (yellow line). (d)–(f) Same as (a)–(c), but for MUCAPE versus SRH500m. SRH500m values for Chile are multiplied by −1 for comparison purposes. Relative distributions are calculated at the nearest grid point and over the three hours prior to each tornado.

Table 2
Number and percent of tornadoes in each region that formed in high-shear, low-CAPE (HSLC) environments.

Region	# of HSLC tornadoes	% of HSLC tornadoes
Chile	20	50.0
WaOr	25	24.5
NoCa	80	34.9
SoCa	38	38.0

3.3. Temporal evolution of convective parameters

The temporal evolution of the mesoscale convective parameters during tornadoes in Chile and along the U.S. west coast was examined for the period from 12 h preceding to 6 h after the reported start time of each tornado. The maximum values at each hour for each parameter in a 0.5° × 0.5° box centered on the tornado (Fig. 6) were analyzed. Differences between mean hourly values of each parameter were tested for statistical significance using a Student's t-test.

In both Chile and along the U.S. west coast, magnitudes of MUCAPE, EBSMU, STP, and SHERBE increase from 9 h before the tornado, peak in the hour or two before the tornado, and then decline afterwards (Fig. 6a,b,d,e). Somewhat unexpectedly, in all regions, the magnitude of SRH500m peaks more than three hours before the tornado, slowly declines through the hour before the tornado, then declines more rapidly afterwards (Fig. 6c); the reasons for this are unknown and require further analysis. Peak values of MUCAPE are greater during tornadoes along the U.S. west coast (>550 J kg^{-1}) than during tornadoes in Chile (<500 J kg^{-1}). In addition, the average increase in MUCAPE in the nine hours preceding a tornado is greater along the U.S. west coast (>350 J kg^{-1} in WaOr and NoCa) than that in Chile (>250 J kg^{-1}) (Fig. 6a). MUCAPE values during tornadoes in both WaOr and especially NoCa are statistically significantly greater than in Chile ($p < 0.05$) in the three hours preceding the tornadoes (open circles in Fig. 6a). In contrast, values of bulk shear, SRH500m, and both composite parameters are larger in Chile than along the U.S. west coast, both in the hours preceding and following the tornado. These differences are statistically significant between Chile and the northern part of the U.S. west coast (WaOr and NoCa) ($p < 0.05$). The increase in these kinematic parameters leading up to the tornado is most pronounced in NoCa and WaOr and least pronounced in SoCa. Values of STP increase the most (>0.07) in the six hours prior to a tornado in Chile. This evolution and short-term variability of the thermodynamic, kinematic, and composite parameters in the hours preceding a tornado are consistent with evolution on mesoscale time scales (Markowski and Richardson, 2011). As such, we recommend that forecasters pay close attention to conditions in near-real time and not necessarily expect parameter values observed early in the day to portend the potential for upcoming severe weather.

3.4. Spatial variability of convective parameters

The spatial variability of convective parameters known to be associated with tornadoes was explored by analyzing their mean values in a domain centered on each report (Fig. 7). This analysis focused on the hour before each reported tornado because the parameters tend to be near or at their maximum values at that hour (see Fig. 6).

The mesoscale environments during tornadoes in Chile and along the U.S. west coast are characterized by localized bands of maximum values of MUCAPE, EBSMU, SRH500m, SHERBE, and STP over or very near (within 50 km of) the tornado report (Fig. 7). These bands tend to orient themselves in a north–south (N–S) configuration in Chile, a southwest–northeast (SW–NE) configuration in WaOr, and a northwest–southeast (NW–SE) configuration in NoCa and SoCa. In each region, the bands of maximum values of the five parameters align approximately parallel to the major axes of the prominent topographic features (Fig. 1). This alignment suggests that the topography of each region is important in spatially organizing the tornadic mesoscale environments.

In Chile, the N–S-oriented bands of the largest EBSMU and SHERBE are located over or less than 50 km to the east of the tornado location, parallel to the major axis of Andes mountains, while the band of greatest SRH500m is displaced nearly 100 km to the east of the tornado. The displacement of the greatest SRH500m towards the Andes is in agreement with the intense barrier jets that develop immediately upstream of the topography during periods of flow blocking by the roughly SSW–NNE-oriented mountain range (Barrett et al., 2009; Viale and Norte, 2009; Viale et al., 2013; Scaff et al., 2017; Marín et al., 2021; Martinez et al., 2024). The area of largest MUCAPE extends from the

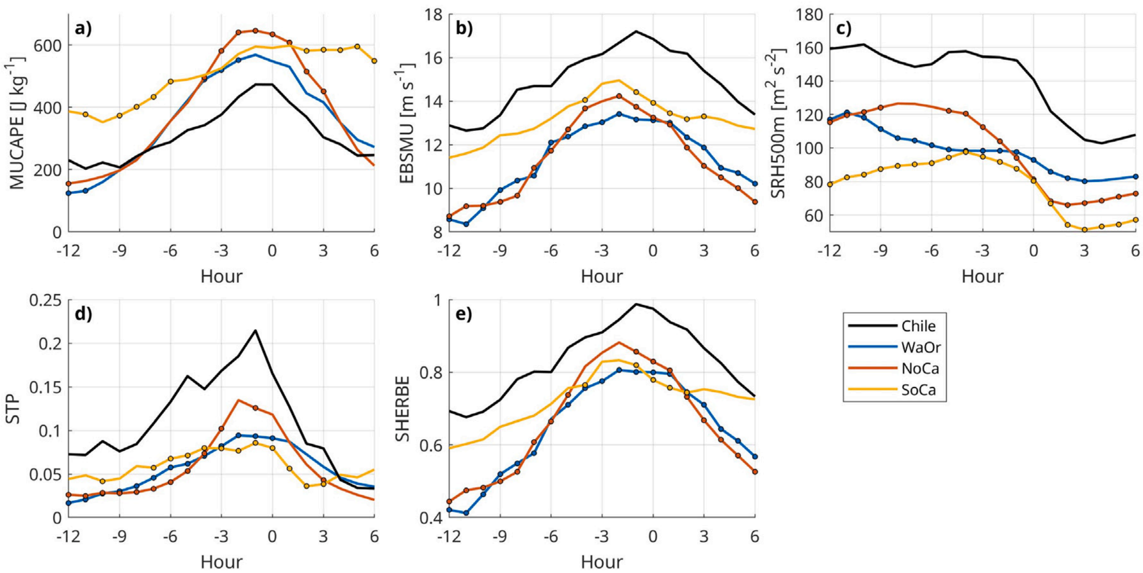

Fig. 6. Temporal evolution of maximum values of (a) MUCAPE, (b) EBSMU, (c) SRH500m, (d) STP, and (e) SHERBE, over the period from 12 h preceding to 6 h after the reported start time of each tornado in a 0.5° × 0.5° latitude–longitude area centered on the tornado location, for Chile (black line), WaOr (blue line), NoCa (red line), and SoCa (yellow line). Open circles indicate values in WaOr, NoCa, and SoCa that are statistically significantly different from Chile at the 95th percentile. The SRH500m and STP for Chile are shown as positive for comparison purposes.

report westward by 50 km upstream, and the band of greatest STP is centered on the tornado. In WaOr and SoCa, the SW–NE and NW–SE bands of maximum values, respectively, are found over or less than 50 km to the southeast of the tornado and also parallel to the major topographic axes of each region. In NoCa, bands of maximum MUCAPE, SHERBE, and STP are centered over the tornado, whereas the bands of maximum EBSMU and SRH500m are displaced 50–75 km to the southeast and northeast, respectively, of the tornado.

In addition to variability in the locations of the bands of maximum values, there is also variability in the magnitudes of the maximum values themselves. The largest magnitudes of MUCAPE (>450 J kg^{-1}) are observed in NoCa, while the smallest magnitudes are observed in Chile (<375 J kg^{-1}). In contrast, the largest values of EBSMU, SRH500m, SHERBE, and STP are observed in Chile, while the smallest magnitudes are observed in SoCa and WaOr. These spatial results could be valuable from a forecasting perspective, as they highlight the bands of maximum values of each convective parameter that help discriminate tornado locations.

3.5. Vertical profiles and hodographs

To understand the vertical structure of the atmosphere associated with tornadoes in each region, we analyzed mean profiles of relative humidity (RH), equivalent potential temperature (θ_e), and u and v wind components at the nearest grid point and hour to each tornado report interpolated from pressure levels to heights above ground. Differences between mean values of RH, θ_e, and wind speed during tornadoes in Chile and along the U.S. west coast were tested for statistical significance using a Student's t-test. Differences in magnitudes of storm motion were tested similarly.

The mean boundary layer is the most saturated in Chile and least saturated in NoCa (Fig. 8a), differences likely associated with greater moisture fluxes in the lowest 2 km in Chile (Table 3) and mean surface temperatures that are 2–3°C cooler in Chile, WaOr, and NoCa than in SoCa (Fig. 8b). Indeed, during tornadoes in SoCa, the entire atmosphere from the surface to 7 km is up to 5 K warmer than in Chile (differences that are statistically significant at the 95th percentile) and up to 6 K warmer than both WaOr and NoCa. All the above result in cloud bases (quantified by the MULCL) ranging from less than 310 m

Table 3
Moisture flux from the surface to 2-km, the lifting condensation level of the most unstable layer (MULCL), mean 0–1 km and 3–6 km lapse rate (LR), and the surface-to-1-km winds, at the nearest grid point and hour to each tornado report in Chile, WaOr, NoCa, and SoCa.

Parameter	Chile	WaOr	NoCa	SoCa
Moisture flux 0–2 km [g s^{-1} m^{-2}]	90	55	45	56
MULCL [m]	308	533	858	823
0–1 km LR [K km^{-1}]	7.6	8.5	9.0	8.1
3–6 km LR [K km^{-1}]	6.8	6.7	6.7	6.5
0–1 km winds [m s^{-1}]	14.3	9.4	7.5	8.1

during tornadoes in Chile to over 820 m during tornadoes in NoCa and SoCa (Table 3). Low cloud bases limit evaporative cooling in the sub-cloud layer and facilitate the vertical stretching of near-ground vertical vorticity (Davies, 2004), both of which are crucial processes for tornadogenesis in environments with low buoyancy (Fischer and Dahl, 2022; Coffer et al., 2023). As such, low LCLs are strongly correlated with tornadic potential in HSLC environments (Coffer et al., 2020). Surface–1-km lapse rates in each region are between 7.6–9 K km^{-1} (Table 3). Each region features weak mid-troposphere lapse rates, smaller than –6.8 K km^{-1} (Table 3 and Fig. 8b), although composite vertical profiles based on reanalysis tend to smooth those features (Brooks et al., 2003; Gensini and Ashley, 2011; Gensini et al., 2014). No convective inhibition (CIN) is present in the mean sounding in any region (not shown). The differences in 0–2-km moisture flux, MULCL, and 0–1-km LR between Chile and the three U.S. west coast regions, and between WaOr and NoCa, are statistically significant at the 95th percentile.

Mean surface winds during tornadoes are the most backed in NoCa and the least backed in WaOr (Fig. 8c). Boundary layer winds in the lowest 1 km are strongest in Chile (14.3 m s^{-1}) and weakest in NoCa (7.5 m s^{-1}) (Table 3), differences that are statistically significant at the 95th percentile. In the middle troposphere, 6-km winds are strongest in Chile (greater than 25 m s^{-1}) and weakest in WaOr (less than 18 m s^{-1}). Differences among the regions are statistically significant (except for SoCa), suggesting that on the synoptic scale, the mid-tropospheric jet associated with tornado environments (Monteverdi et al., 2003; Barrett et al., 2020) is stronger in Chile than in the other regions.

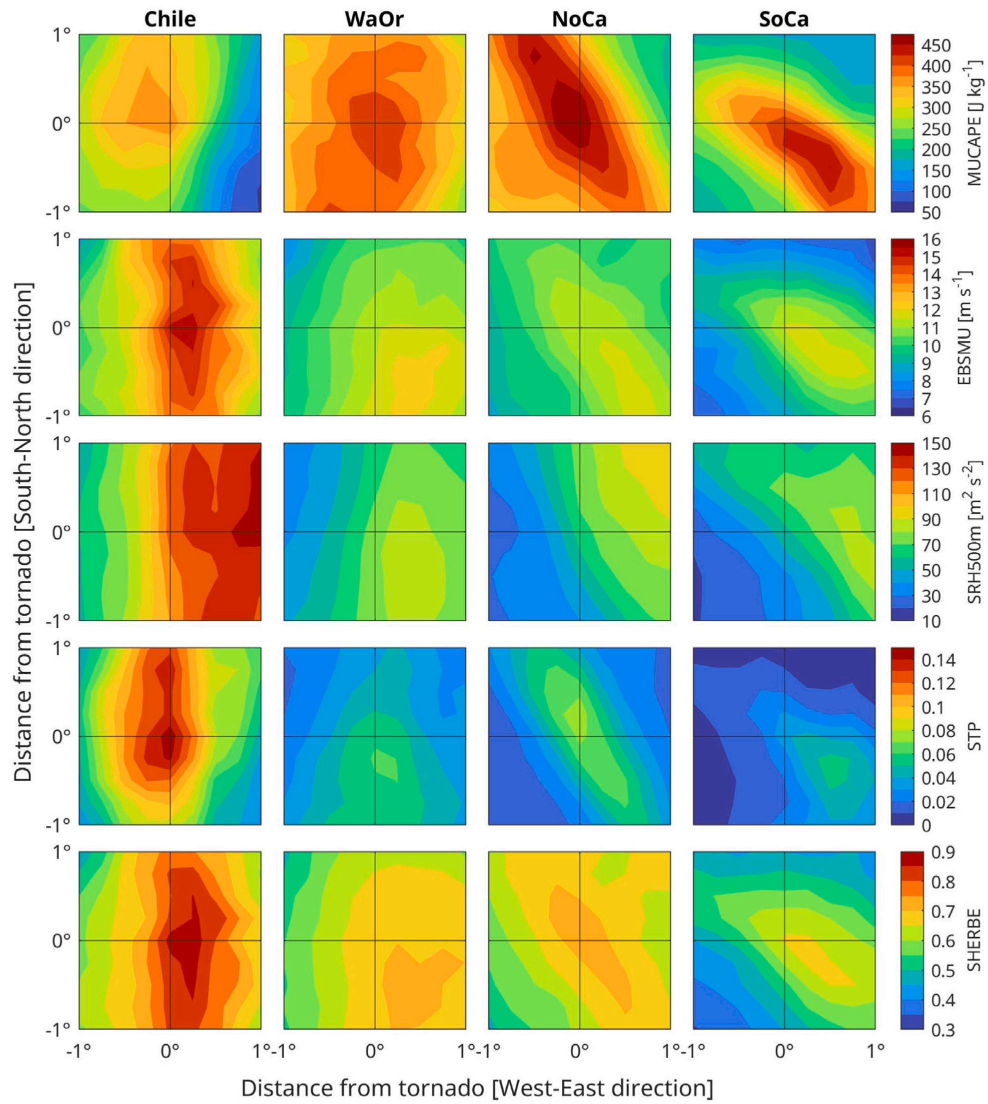

Fig. 7. Mean spatial distribution of MUCAPE, EBSMU, SRH500m, STP, and SHERBE, centered on each report, in the hour before a tornado in Chile, WaOr, NoCa, and SoCa. Values of SRH500m and STP in Chile are multiplied by −1 for ease of comparison.

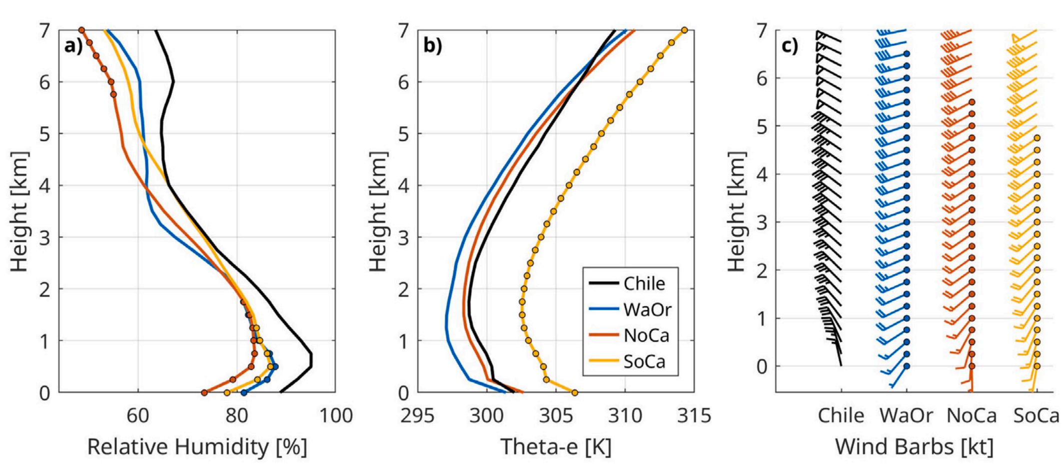

Fig. 8. Mean vertical profiles of (a) relative humidity (RH), (b) equivalent potential temperature (θ_e), and (c) horizontal winds at the nearest grid point and hour to each tornado report in Chile (black), WaOr (blue), NoCa (red), and SoCa (yellow). Open circles indicate height levels in WaOr, NoCa, and SoCa where values are statistically significantly different from Chile at the 95th percentile.

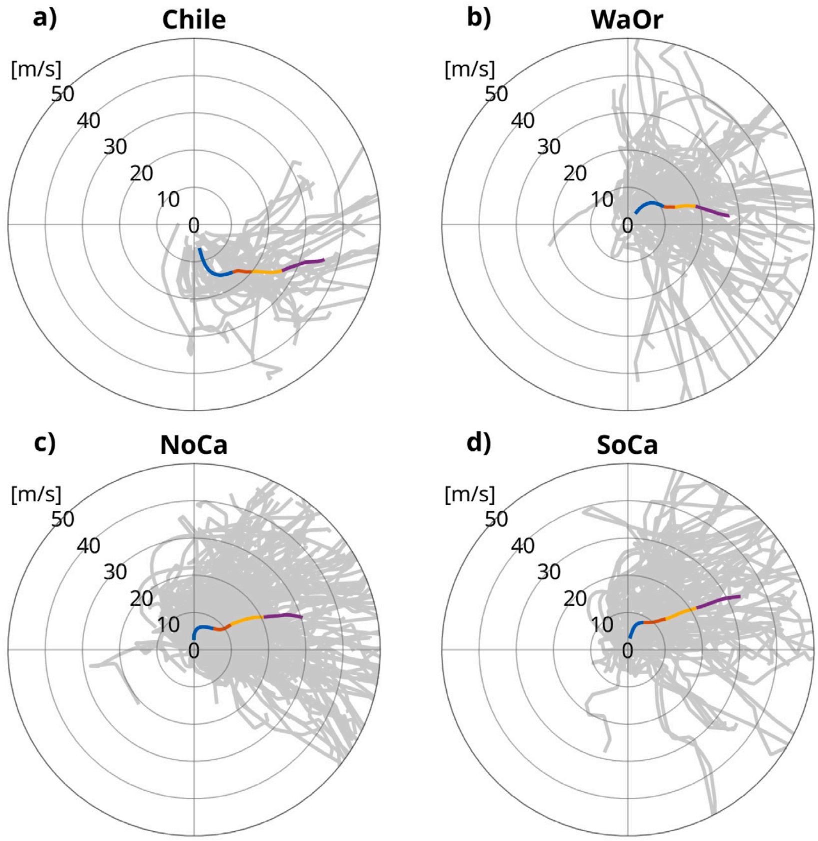

Fig. 9. Hodographs at the nearest grid point and hour to each tornado report (gray lines) in (a) Chile, (b) WaOr, (c) NoCa, and (d) SoCa. The colored lines represent the mean hodograph for each studied region, color-coded to indicate the 0–1 km (blue), 1–3 km (red), 3–6 km (yellow), and 6–9 km (purple) height segments.

Mean hodographs in each region feature curvature that favors cyclonically rotating storms (Doswell, 1991) (Fig. 9), and mean turning and hodograph size in the lowest 1-km are largest in Chile and smallest in SoCa. The least amount of spread in hodograph shape is observed for Chile, and the greatest is observed for WaOr. In WaOr, hodographs are oriented both predominantly northward and southward, indicating that tornadoes occur there during periods of both southerly and northerly deep-layer shear (Fig. 9b). In contrast, in Chile, hodographs are oriented predominately southeastward, indicating that tornadoes there occur predominately when the deep-layer shear vector is northwesterly (Fig. 9a). These different hodograph shapes suggest that the synoptic-scale patterns during tornadoes are most variable in WaOr and least variable in Chile. Bunker's storm motions for the left-moving storm in Chile and the right-moving storm in the U.S. reflect the mean wind profiles during tornadoes in each region (Bunkers et al., 2000). Storms move fastest in Chile (17.2 m s^{-1}) and slower in each of the regions along the U.S. west coast (15.2, 14.5, and 15.6 m s^{-1}, respectively, in WaOr, NoCa, and SoCa). These differences indicate that winds through the lower and middle troposphere are faster during tornadoes in Chile. However, the differences are statistically significant only for NoCa ($p = 0.10$, 0.02, and 0.12, respectively).

3.6. Lightning activity

In this section, we describe the spatial variability of lightning activity associated with tornadic storms in three of the four regions (Chile, WaOr and NoCa). Flash density for SoCa is not shown because data were only available for five tornadoes there. Despite the limited period of availability from 2017–2023, the novelty of these results, particularly for Chile, makes their presentation and discussion noteworthy.

In Chile, lightning was detected by the GLM within 1° latitude–longitude and between one hour before and after the time of 19 of the 23 tornadoes reported between 2017–2023. The flash density distribution shows lightning activity mostly concentrated in a NW–SE band over and to the west of the report (Fig. 10a), approximately coinciding with the area of highest CAPE over and to the west of the tornado (Fig. 7). In WaOr, lightning was detected during 11 of the 17 tornadoes reported between 2017–2023 (Fig. 10b), and lightning flashes predominantly occur in a W–E oriented band centered on the tornado, although they also occur to the SE of the report. In NoCa, lightning was detected during 17 of the 25 reported tornadoes (Fig. 10c). Lightning flashes in NoCa occur throughout the 2° × 2° domain, also somewhat oriented parallel to the area of highest CAPE over NoCa (Fig. 7), with the flash density greatest over and to the northwest of the tornado. There appear to be more lightning flashes per storm associated with tornadic storms in NoCa (even more than 1000 flashes) than in Chile and WaOr, although that difference was not tested for statistical significance. While the greatest concentration of flashes is within 0.2° latitude–longitude of the reported tornado in all regions, flashes in Chile and NoCa extend up to 1° from the tornado location.

Lightning activity is relatively rare both in Chile and along the U.S. west coast, particularly in the cool season. For example, Montana et al. (2021) found only 5–7 thunderstorm days per year in south-central Chile outside of the immediate Andes mountains, with only 15%–20% of those days occurring in the cool season. Van Wagtendonk and Cayan (2008) found similarly low flash rates, less than 5 strikes yr^{-1} 100^{-1} km^{-2}, for both NoCa and SoCa. It is important to note that both of those studies used terrestrial lightning detection networks, which have detection paradigms that are distinct from the GLM sensor. Given that tornadoes are also rare events in these regions, and that lightning is detected in near-real-time on finer spatial and temporal

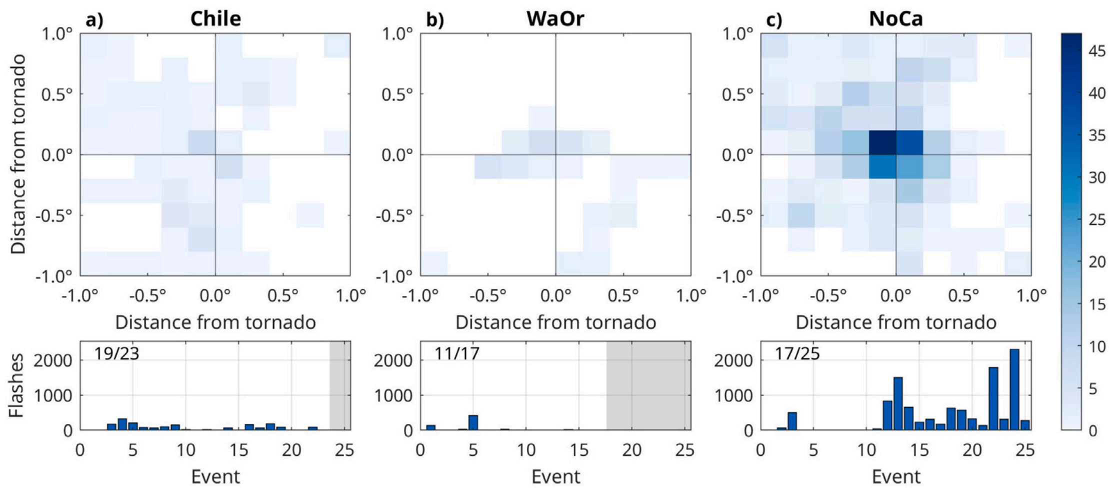

Fig. 10. GLM flash density (shading, average number of flashes per tornado) and flash count (bars) within 1° latitude–longitude and one hour of reported tornadoes in (a) Chile, (b) WaOr, and (c) NoCa between 2017–2023. Flash density for SoCa is not shown because the sample size is small.

scales than potentially available for other diagnostic parameters, we explored whether the number of flashes associated with tornadic storms showed any relationship with the magnitude of the analyzed convective parameters in the studied regions. Any relationship with lightning flash activity could thus serve as a proxy for tornadic storm potential.

Weak (Wilks, 2011) positive relationships were found between the number of flashes detected in each storm and the maximum values of MUCAPE and SRH500m, with a Pearson product-moment correlation coefficient of 0.31 ($p = 0.024$) (Fig. 11a,c). On the other hand, moderate positive correlations between the number of flashes and the maximum values of EBSMU, STP, and SHERBE were found, with correlation coefficients of 0.47, 0.46, and 0.59, respectively ($p < 0.001$), suggesting that more flashes tend to occur when shear is stronger. These correlations explain approximately 22%, 21%, and 35% of the flash count variability in the tornadic environments (Fig. 11b,d,e). Observed lightning activity may thus serve as another mesoscale parameter, alongside instability and shear, to consider when evaluating tornado potential in the real-time forecast setting.

To further understand lightning activity during tornadoes in Chile and along the U.S. west coast, we analyzed the mean spatial distributions of the Significant Hail Parameter (SHIP; NOAA, 2022; Czernecki et al., 2019). This analysis was motivated by a number of studies showing that lightning activity in severe storms positively correlates with hail in the storm (Wapler, 2017; Farnell et al., 2017; Poręba et al., 2022; Brunet and Brimelow, 2024). We examined SHIP in the hour immediately preceding each tornado in Chile, WaOr, and NoCa for two cases: one for all tornadoes and one for only the tornadoes with lightning activity. We found that tornadoes with lightning activity have larger values of SHIP than the broader population, a result that holds in all regions (Fig. 12). Furthermore, the area of maximum SHIP in each region is offset spatially from the area of maximum lightning density (Fig. 10) by approximately 50 km to the *N* in Chile and approximately 35 km to the SW in both WaOr and NoCa, in agreement with Zhang and Ni (2026). The greatest values of SHIP are located in NoCa, coinciding with the largest density of lightning flashes among the three regions. It is possible that both lightning activity and hail are measures of updraft intensity and thus could serve as indicators of tornado potential in Chile and along the U.S. west coast. However, that was not explored further. A detailed spatio-temporal analysis of hail across the studied regions is suggested for future research.

To the authors' knowledge, this is the first analysis of lightning activity for tornadoes in either Chile or along the U.S. west coast. Given that lightning activity seems to be present in 64.7%–82.4% of tornadoes in each region, and that between 24.5%–50.0% of tornadoes in each region occur in HSLC environments, this result suggests that lightning could be somewhat common in tornado environments in Chile and along the U.S. west coast. This result is different from McAvoy et al. (2000), who found no significant lightning activity during tornadoes in HSLC environments. However, as previously mentioned, this disagreement may be due to the different lightning datasets and detection methodologies in both studies.

4. Discussion and conclusions

In this study, we analyzed the mesoscale conditions during tornadoes in Chile and along the U.S. west coast from 1980–2023. We used the ERA5 reanalysis to explore the variability of convective parameters that have been shown to have skill at discriminating tornadic from non-tornadic storms. We focused our analysis on tornadoes in south-central Chile and in three domains along the U.S. west coast: Washington–Oregon (WaOr), northern California (NoCa), and southern California (SoCa).

Previous studies have shown that tornadoes along the U.S. west coast occur more frequently in the afternoon hours and less frequently at night and in the early morning hours. Tornadoes in Chile show the same behavior. Tornadoes in Chile, NoCa, and SoCa occur primarily in the fall and winter months, while those in WaOr occur mostly in the spring and fall months. The seasonality of the analyzed convective parameters is consistent with that of tornado frequency in Chile and across all three regions along the U.S. west coast. Of note is the good correspondence between the monthly mean STP and the frequency of tornadoes, particularly in Chile and NoCa, despite the original intent for STP to distinguish environments supportive of significant ([E]F-2+) tornadoes. Nevertheless, there is some misalignment between seasonal peaks in thermodynamic and kinematic parameters, particularly in WaOr, highlighting the complexity of assessing the mesoscale environments associated with tornadoes and the need to consider both CAPE- and shear-based parameters.

The values of STP and SHERBE found during tornadoes in Chile and along the west coast of the U.S. are similar to those found for HSLC tornadoes in other regions. For example, Brown et al. (2021) found average STP values less than 0.5 during HSLC tornadoes in the southeastern U.S., particularly before the early-evening boundary layer transition, confirming that relatively low magnitudes of STP are common during tornado events where instability is weak. Furthermore, Bărăscu et al. (2026) found STP values regularly less than 0.2 in the hours leading up to tornadoes in Romania and noted that the STP provides operational forecasting utility when examined alongside other

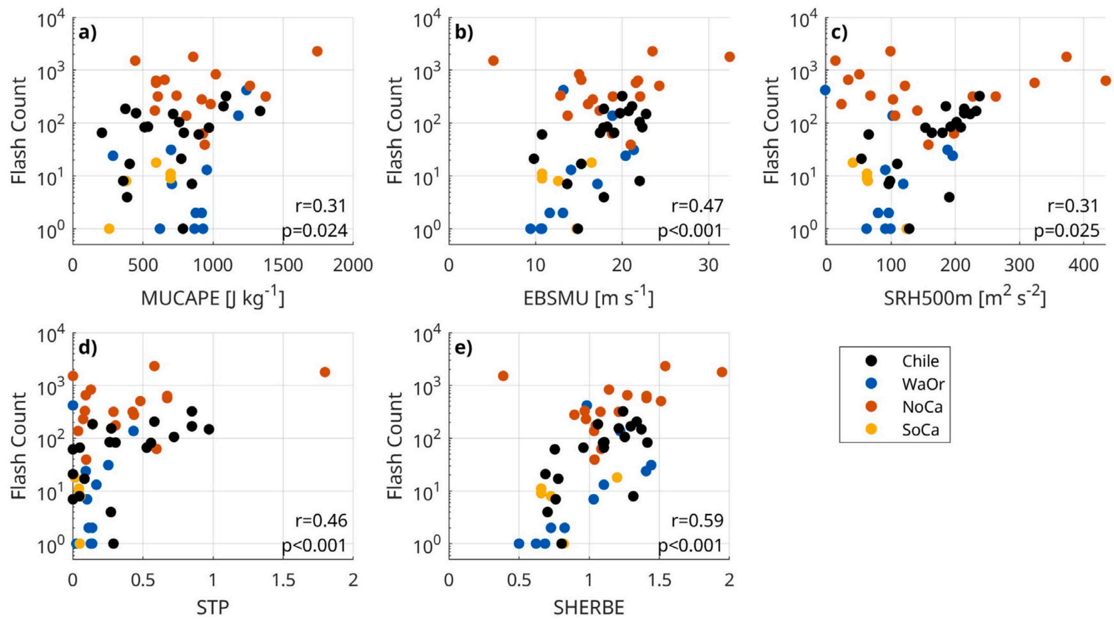

Fig. 11. Number of flash counts (on a natural logarithm scale) versus the maximum values of (a) MUCAPE, (b) EBSMU, (c) SRH500m, (d) STP, and (e) SHERBE, in a 0.5° × 0.5° latitude–longitude domain centered on the report during three hours before each tornado with at least one detected lighting flash, in Chile (black), WaOr (blue), NoCa (red), and SoCa (yellow). The correlation coefficient (r) between the natural log of counts and the corresponding variable, and its statistical significance (p), are given in the lower right. Correlations consider all data points in all regions.

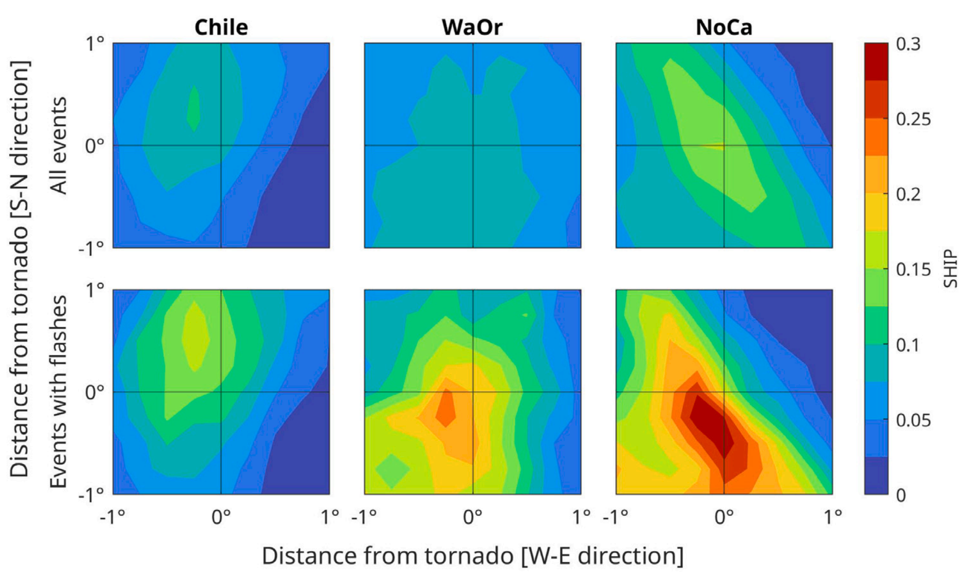

Fig. 12. Mean spatial distribution of the Significant Hail Parameter (SHIP), centered on each report, in the hour before a tornado, for all tornadoes between 1980–2023 (“all events”) and only tornadoes between 2017–2023 with flashes detected by the GLM (“events with flashes”) in Chile, WaOr, and NoCa.

convective parameters. The analyses here for Chile and the U.S. west coast confirm that relatively small values of STP can still identify environments favorable for tornadoes. For the case of SHERBE, Campbell et al. (2024) found that more than half of the HSLC tornadoes in the southeastern U.S. form in environments with less than 100 J kg^{-1} of MUCAPE and with SHERBE greater than 0.5. Dynamically, SHERBE is similar to STP in that it measures the combined contributions of environmental wind shear and instability. However, instead of capturing instability through CAPE, which is strongly sensitive to surface air and dew point temperature (Emanuel, 2023), SHERBE captures it through low- and mid-level lapse rates (Sherburn and Parker, 2014). Steep low-level lapse rates correspond to stronger convection, even when instability is marginal (McCaul and Weisman, 2001), and steep mid-level lapse rates have shown high correlation with significant severe weather outbreaks (Banacos and Ekster, 2010) and tornadogenesis (Godfrey et al., 2004; Parker, 2012). Physically, steep low- and mid-level lapse rates both contribute to storm strength and tornadogenesis through intensification of convective updrafts (McCaul and Weisman, 2001).

Approximately 50% of tornadoes in Chile were found in HSLC environments, compared with only 25%–38% of tornadoes along the U.S. west coast. Tornadoes that form in HSLC environments are often associated with quasi-linear convective systems or low-topped convection (Davis and Parker, 2014; Anderson-Frey et al., 2016), particularly during the cool season when the tropopause height is climatologically low (Monteverdi and Quadros, 1994). In the May 2019 outbreak in Chile, Barrett et al. (2020) and Vicencio et al. (2021) concluded that the tornadoes formed from discrete and semi-discrete supercellular convection ahead of a passing mid- and upper-tropospheric trough and accompanying surface fronts. Some very recent results suggest that tornadoes in Chile form in both frontal and post-frontal environments (not shown). However, to date, neither the synoptic patterns nor the storm modes have been systematically analyzed for any other recent tornado event in Chile. This is suggested as an area for future research. In NoCa, Blier and Batten (1994) suggest that nonsupercell processes, such as intense horizontal shear along fronts (Carbone, 1983) or favorable interactions between storms and preexisting horizontal vorticity associated with outflows or sea-breeze boundaries (Monteverdi et al., 2001), could be responsible for the majority of tornadoes there. Monteverdi et al. (1988) and Monteverdi et al. (2003) found that tornadoes in NoCa typically occur in the post-frontal region beneath a 300-hPa jet streak associated with the passage of an upper-tropospheric trough in environments with deep-layer shear vectors that favor supercellular convection. However, a similar synoptic-climatology of tornado environments does not exist for WaOr, nor has one been recently revisited for either NoCa or SoCa; this is suggested as another area for future research.

Topographically induced near-surface flows parallel to the major axis of the Sierra Nevada mountains both greatly increase the low-level shear available to storms in NoCa and contribute to substantial near-surface warm advection there (Hanstrum et al., 2002). This mesoscale generation of large magnitudes of vertical wind shear by terrain-influenced circulations in NoCa is very similar to the barrier jets induced by flow blocking by the Andes that Marín et al. (2021) found to significantly increase the low-level vertical shear available to storms in Chile. It is thus at least plausible that terrain-induced surface flows are a contributing mesoscale factor favoring tornadogenesis in WaOr and SoCa, although that hypothesis, to the authors' knowledge, has not been tested for those regions. Regardless, it is clear that once thunderstorms have initiated, strongly veering wind shear profiles in the three U.S. regions — and strongly backing profiles in Chile — contribute to dynamically-induced perturbation pressure gradient forces that subsequently strengthen the convective updrafts (Rotunno and Klemp, 1982; McCaul, 1993; Davies-Jones et al., 2001; Dawson et al., 2016). When these accelerations are located in layers with large lapse rates, such as those with SHERBE values approaching 1, they can compensate for meager CAPE and augment the buoyancy force by a factor of two or more (Wicker and Cantrell, 1996; Hanstrum et al., 2002; Monteverdi et al., 2003).

Values of MUCAPE, EBSMU, SHERBE, and STP increase, on average, in all regions from nine hours before to the hour of the tornado. The increase in MUCAPE is larger along the U.S. west coast, but the increase in the other variables is larger in Chile and NoCa, particularly for STP in Chile. Localized bands of maximum values of these parameters are found over or within 50 km of the tornado report and are aligned with the major axes of the most prominent topographical feature of each region. These mesoscale details, both temporal and spatial, could help operational forecasters in locating environments potentially favorable for tornadoes.

The vertical structure of the atmosphere associated with tornadoes in the four regions exhibits notable features. Tornadic storms in Chile have the lowest cloud base, the most saturated environment, and the strongest low-level horizontal moisture fluxes of the four regions. On the other hand, low-level moisture fluxes are weakest in NoCa, giving NoCa the driest boundary layer and highest cloud bases. The mesoscale environments in Chile show the strongest winds over the depth of the atmospheric column, giving Chile the largest EBSMU values among the studied regions. In addition, the largest magnitudes of storm-relative helicity also occur in Chile, and theoretical storm motions there are fastest and largely parallel to the Andes mountains. On days with tornadoes, very favorable kinematic conditions and strong lapse rates in Chile help to overcome relatively weak atmospheric instability to support tornadogenesis.

Tornadic storms in northern California have a greater density of lightning flashes clustered closer to the tornado report than storms in Chile or WaOr. This may be the result of the interplay of several interrelated factors in NoCa, such as greater instability, higher aerosol concentrations due to increased pollution in a more industrialized region, higher LCLs, and consequently, higher cloud bases (Rakov and Uman, 2003), all of which favor the production of more lightning flashes during tornadic storms. Moreover, a greater fraction of NoCa tornadoes occur in months which are thermodynamically biased towards greater charge separation and lightning production (Williams et al., 2005). On the other hand, tornadic storms in Chile are characterized by lower atmospheric instability, possibly less polluted air, lower cloud bases, and thus relatively less lightning activity. In addition, Pozo et al. (2023) found that cold fronts with higher freezing levels are more frequent in May and June (when tornado frequency is highest in Chile), which is an unfavorable condition for lightning production.

Finally, limitations of the Chilean tornado database preclude analysis of potential long-term trends there. While Marín et al. (2024) did not find long-term trends in the number of favorable tornadic environments in south-central Chile between 1959 and 2021, they did find statistically significant variability in the number of favorable tornadic environments during the first half of their study (1959–1989). They suggest this variability may reflect possible modulation by large-scale circulations such as the El Niño Southern Oscillation (ENSO), the Pacific Decadal Oscillation (PDO), the Southern Annular Mode (SAM), or the Madden-Julian Oscillation (MJO). All of these modes of variability have been shown to have notable impacts on large-scale climate patterns in South America and Chile (Barrett et al., 2012; Juliá et al., 2012; Jacques-Coper and Garreaud, 2015; Campos and Rondanelli, 2023). Indeed, Barrett et al. (2020) found that the evolution of the large-scale tropospheric circulation over the second half of May 2019, coincident with the tornado outbreak of 30–31 May 2019 in south-central Chile, was partly associated with a Rossby wave train excited during phases 1 and 2 of a strong MJO event. Determining possible associations between large-scale global circulations and tornadoes in Chile is suggested as an area of future research. In the U.S., most studies analyzing long-term trends in tornado activity and the influence of large-scale circulations have focused on regions with greater tornado frequency, such as the Great Plains, Midwest, and Southeast (Gensini and Brooks, 2018; Nouri et al., 2021), leaving as uncertain possible trends in tornado activity along the west coast. However, since ENSO and the PDO have been shown to influence the hydroclimate of the U.S. west coast (Patricola et al., 2020; Maher et al., 2022), the role of these global circulations on tornadoes occurring in this region should also be studied in more detail.

CRediT authorship contribution statement

Julio C. Marín: Writing – review & editing, Writing – original draft, Methodology, Investigation, Conceptualization. **Bradford S. Barrett:** Writing – review & editing, Writing – original draft, Methodology, Formal analysis, Conceptualization. **Felipe Gutiérrez Cotapos:** Writing – review & editing, Visualization, Methodology, Investigation, Formal analysis, Data curation. **Diana Pozo:** Writing – review & editing, Investigation, Conceptualization.

Declaration of competing interest

The authors declare that they have no known competing financial interests or personal relationships that could have appeared to influence the work reported in this paper.

Acknowledgments

Marín and Pozo acknowledge support from the Centro de Estudios Atmosféricos y Cambio Climático (CEACC), Universidad de Valparaíso. Marín and Pozo acknowledge support from ANID/Fondecyt Project 1252128.

Data availability

Data will be made available on request.

References

Aceituno, P., Boisier, J.P., Garreaud, R., Rondanelli, R., Rutllant, J.A., 2020. Climate and weather in Chile. In: Water Resources of Chile. Springer, pp. 7–29.

Allen, J.T., Allen, E.R., Richter, H., Lepore, C., 2021. Australian tornadoes in 2013: Implications for climatology and forecasting. Mon. Weather Rev. 149 (5), 1211–1232.

Allen, J.T., Karoly, D.J., 2014. A climatology of Australian severe thunderstorm environments 1979–2011: Inter-annual variability and ENSO influence. Int. J. Climatol. 34 (1).

Anderson-Frey, A.K., Richardson, Y.P., Dean, A.R., Thompson, R.L., Smith, B.T., 2016. Investigation of near-storm environments for tornado events and warnings. Weather. Forecast. 31 (6), 1771–1790.

Anderson-Frey, A.K., Richardson, Y.P., Dean, A.R., Thompson, R.L., Smith, B.T., 2019. Characteristics of tornado events and warnings in the southeastern United States. Weather. Forecast. 34 (4), 1017–1034.

Antonescu, B., Schultz, D.M., Holzer, A., Groenemeijer, P., 2017. Tornadoes in Europe: An underestimated threat. Bull. Am. Meteorol. Soc. 98 (4), 713–728.

Aránguiz, R., Saez, B., Gutiérrez, G., Oyarzo-Vera, C., Nuñez, E., Quiñones, C., Bobadilla, R., Bull, M.T., 2020. Damage assessment of the may 31st, 2019, Talcahuano tornado, Chile. Int. J. Disaster Risk Reduct. 50, 101853.

Ashley, W.S., Krmenec, A.J., Schwantes, R., 2008. Vulnerability due to nocturnal tornadoes. Weather. Forecast. 23 (5), 795–807.

Avolio, E., Miglietta, M.M., 2023. A comparative analysis of two Mediterranean tornado hotspots. Atmosphere 14 (1), 189.

Banacos, P.C., Ekster, M.L., 2010. The association of the elevated mixed layer with significant severe weather events in the northeastern United States. Weather. Forecast. 25 (4), 1082–1102.

Bărăscu, A., Antonescu, B., Ene, D., Ionita, M., Rusz, O., Kühne, T., Bell, A., 2026. An updated tornado climatology for Romania. Mon. Weather Rev. 154 (4), 625–642.

Barrett, B.S., Carrasco, J.F., Testino, A.P., 2012. Madden–Julian oscillation (MJO) modulation of atmospheric circulation and Chilean winter precipitation. J. Clim. 25 (5), 1678–1688.

Barrett, B.S., Garreaud, R., Falvey, M., 2009. Effect of the andes cordillera on precipitation from a midlatitude cold front. Mon. Weather Rev. 137 (9), 3092–3109.

Barrett, B.S., Hameed, S., 2017. Seasonal variability in precipitation in central and southern Chile: Modulation by the south Pacific high. J. Clim. 30 (1), 55–69.

Barrett, B.S., Krieger, D.B., Barlow, C.P., 2011. Multiday circulation and precipitation climatology during winter rain events of differing intensities in central Chile. J. Hydrometeorol. 12 (5), 1071–1085.

Barrett, B.S., Marin, J.C., Jacques-Coper, M., 2020. A multiscale analysis of the tornadoes of 30–31 may 2019 in south-central Chile. Atmos. Res. 236, 104811. http://dx.doi.org/10.1016/j.atmosres.2019.104811.

Bastías-Curivil, C., Rondanelli, R., Vicencio, J., Matus, F., Caballero, V., Muñoz, F., et al., 2024. Tornadoes and waterspouts in Chile/Tornados y Trombas en Chile. Dataset http://dx.doi.org/10.6084/m9.figshare.25119566.v3.

Blier, W., Batten, K.A., 1994. On the incidence of tornadoes in California. Weather. Forecast. 9 (3), 301–315.

Braun, S.A., Monteverdi, J.P., 1991. An analysis of a mesocyclone–induced tornado occurrence in northern California. Weather. Forecast. 6 (1), 13–31.

Bridenstine, P.V., Darden, C.B., Burks, J., Goodman, S.J., 2005. The application of total lightning data in the warning decision making process. In: Preprints, 2nd Conf. on Meteorological Applications of Lightning Data, San Diego, CA, Amer. Meteor. Soc. CD-ROM P. Vol. 1.

Brooks, H.E., 2009. Proximity soundings for severe convection for Europe and the United States from reanalysis data. Atmos. Res. 93 (1–3), 546–553.

Brooks, H.E., Carbin, G.W., Marsh, P.T., 2014. Increased variability of tornado occurrence in the United States. Science 346 (6207), 349–352.

Brooks, H.E., Lee, J.W., Craven, J.P., 2003. The spatial distribution of severe thunderstorm and tornado environments from global reanalysis data. Atmos. Res. 67, 73–94.

Brotzge, J.A., Nelson, S.E., Thompson, R.L., Smith, B.T., 2013. Tornado probability of detection and lead time as a function of convective mode and environmental parameters. Weather. Forecast. 28 (5), 1261–1276. http://dx.doi.org/10.1175/WAF-D-12-00119.1.

Brown, M.C., Nowotarski, C.J., Dean, A.R., Smith, B.T., Thompson, R.L., Peters, J.M., 2021. The early evening transition in southeastern US tornado environments. Weather. Forecast. 36 (4), 1431–1452.

Brunet, D., Brimelow, J., 2024. A hail climatology for Canada using a lightning proxy. J. Appl. Meteorol. Clim. 63 (10), 1227–1240.

Bunkers, M.J., Klimowski, B.A., Zeitler, J.W., Thompson, R.L., Weisman, M.L., 2000. Predicting supercell motion using a new hodograph technique. Weather. Forecast. 15 (1), 61–79.

Caballero-Morán, V., Rondanelli, R., 2025. Tornado seasonality in central-southern Chile. Geophys. Res. Lett. 52 (1), e2024GL110900.

Campbell, T.A., Lackmann, G.M., Molina, M.J., Parker, M.D., 2024. Severe convective storms in limited instability organized by pattern and distribution. Weather. Forecast. 39 (1), 217–240.

Campos, D., Rondanelli, R., 2023. ENSO-related precipitation variability in Central Chile: The role of large scale moisture transport. J. Geophys. Res.: Atmos. 128 (17), e2023JD038671.

Carbone, R.E., 1983. A severe frontal rainband. Part II: Tornado parent vortex circulation. J. Atmos. Sci. 40 (11), 2639–2654.

Chalmers, Z.A., Parker, M.D., 2026. Variability in high-shear, low-CAPE QLCS environments in the southeastern United States. Weather. Forecast. 41 (6), 1093–1117.

Childs, S.J., Schumacher, R.S., Allen, J.T., 2018. Cold-season tornadoes: Climatological and meteorological insights. Weather. Forecast. 33 (3), 671–691.

Clark, M.R., 2009. The southern England tornadoes of 30 december 2006: Case study of a tornadic storm in a low CAPE, high shear environment. Atmos. Res. 93 (1–3), 50–65.

Clark, A.J., 2017. Toward predicting US tornadoes in the late 21st century. In: Climate Extremes: Patterns and Mechanisms. Wiley Online Library, pp. 361–369.

Coffer, B.E., Parker, M.D., 2015. Impacts of increasing low-level shear on supercells during the early evening transition. Mon. Weather Rev. 143 (5), 1945–1969.

Coffer, B.E., Parker, M.D., Coniglio, M.C., Homeyer, C.R., 2025. Supercell environments using GridRad-severe and the HRRR: Addressing discrepancies between prior tornado datasets. Weather. Forecast. 40 (8), 1405–1428.

Coffer, B.E., Parker, M.D., Peters, J.M., Wade, A.R., 2023. Supercell low-level mesocyclones: Origins of inflow and vorticity. Mon. Weather Rev. 151 (9), 2205–2232.

Coffer, B.E., Parker, M.D., Thompson, R.L., Smith, B.T., Jewell, R.E., 2019. Using near-ground storm relative helicity in supercell tornado forecasting. Weather. Forecast. 34 (5), 1417–1435. http://dx.doi.org/10.1175/WAF-D-19-0115.1.

Coffer, B.E., Taszarek, M., Parker, M.D., 2020. Near-ground wind profiles of tornadic and nontornadic environments in the United States and Europe from ERA5 reanalyses. Weather. Forecast. 35 (6), 2621–2638.

Cook, A.R., Leslie, L.M., Parsons, D.B., Schaefer, J.T., 2017. The impact of El Niño–Southern oscillation (ENSO) on winter and early spring US tornado outbreaks. J. Appl. Meteorol. Clim. 56 (9), 2455–2478.

Cook, A.R., Schaefer, J.T., 2008. The relation of El Niño–Southern oscillation (ENSO) to winter tornado outbreaks. Mon. Weather Rev. 136 (8), 3121–3137.

Czernecki, B., Taszarek, M., Marosz, M., Półrolniczak, M., Kolendowicz, L., Wyszogrodzki, A., Szturc, J., 2019. Application of machine learning to large hail prediction-The importance of radar reflectivity, lightning occurrence and convective parameters derived from ERA5. Atmos. Res. 227, 249–262.

Dai, A., Wigley, T., 2000. Global patterns of ENSO-induced precipitation. Geophys. Res. Lett. 27 (9), 1283–1286.

Davies, J.M., 2004. Estimations of CIN and LFC associated with tornadic and nontornadic supercells. Weather. Forecast. 19 (4), 714–726.

Davies, J.M., Johns, R.H., 1993. Some wind and instability parameters associated with strong and violent tornadoes: 1. Wind shear and helicity. Geophys. Monogr. Ser. 79, 573–582.

Davies-Jones, R., 2015. A review of supercell and tornado dynamics. Atmos. Res. 158, 274–291.

Davies-Jones, R., Trapp, R.J., Bluestein, H.B., 2001. Tornadoes and tornadic storms. In: Severe Convective Storms. Springer, pp. 167–221.

Davis, J.M., Parker, M.D., 2014. Radar climatology of tornadic and nontornadic vortices in high-shear, low-CAPE environments in the mid-Atlantic and southeastern United States. Weather. Forecast. 29 (4), 828–853.

Dawson, D.T., Xue, M., Shapiro, A., Milbrandt, J.A., Schenkman, A.D., 2016. Sensitivity of real-data simulations of the 3 may 1999 Oklahoma city tornadic supercell and associated tornadoes to multimoment microphysics. Part II: Analysis of buoyancy and dynamic pressure forces in simulated tornado-like vortices. J. Atmos. Sci. 73 (3), 1039–1061.

de Lima Nascimento, E., Held, G., Gomes, A.M., 2014. A multiple-vortex tornado in southeastern Brazil. Mon. Weather Rev. 142 (9), 3017–3037.

Dean, A., Schneider, R., 2008. Forecast challenges at the NWS storm prediction center relating to the frequency of favorable severe storm environments.

Deitch, M.J., Sapundjieff, M.J., Feirer, S.T., 2017. Characterizing precipitation variability and trends in the world's Mediterranean-climate areas. Water 9 (4), 259.

Dong, B., Dai, A., 2015. The influence of the interdecadal Pacific oscillation on temperature and precipitation over the globe. Clim. Dyn. 45 (9), 2667–2681.

Doswell, III, C.A., 1991. A review for forecasters on the application of hodographs to forecasting severe thunderstorms. Natl. Wea. Dig 16 (1), 2–16.

Doswell, III, C.A., Moller, A.R., Brooks, H.E., 1999. Storm spotting and public awareness since the first tornado forecasts of 1948. Weather. Forecast. 14 (4), 544–557.

Edwards, R., Elliott, M.S., Marsh, P.T., Speheger, D., 2022. Errors, oddities and artifacts in US Tornado data, 1995–2020. In: 30th Conference on Severe Local Storms. AMS.

Emanuel, K., 2023. On the physics of high CAPE. J. Atmos. Sci. 80 (11), 2669–2683.

Farnell, C., Rigo, T., Pineda, N., 2017. Lightning jump as a nowcast predictor: Application to severe weather events in Catalonia. Atmos. Res. 183, 130–141.

Fischer, J., Dahl, J.M., 2022. Transition of near-ground vorticity dynamics during tornadogenesis. J. Atmos. Sci. 79 (2), 467–483.

Fischer, J., Dahl, J.M., Coffer, B.E., Houser, J.L., Markowski, P.M., Parker, M.D., Weiss, C.C., Schueth, A., 2024. Supercell tornadogenesis: Recent progress in our state of understanding. Bull. Am. Meteorol. Soc. 105 (7), E1084–E1097.

Gensini, V.A., Ashley, W.S., 2011. Climatology of potentially severe convective environments from the North American regional reanalysis. E-J. Sev. Storms Meteorol. 6 (8), 1–40.

Gensini, V.A., Brooks, H.E., 2018. Spatial trends in United States tornado frequency. NPJ Clim. Atmos. Sci. 1 (1), 38. http://dx.doi.org/10.1038/s41612-018-0048-2.

Gensini, V.A., Converse, C., Ashley, W.S., Taszarek, M., 2021. Machine learning classification of significant tornadoes and hail in the United States using ERA5 proximity soundings. Weather. Forecast. 36 (6), 2143–2160. http://dx.doi.org/10.1175/WAF-D-21-0056.1.

Gensini, V.A., Mote, T.L., Brooks, H.E., 2014. Severe-thunderstorm reanalysis environments and collocated radiosonde observations. J. Appl. Meteorol. Clim. 53 (3), 742–751.

Godfrey, E.S., Trapp, R.J., Brooks, H.E., 2004. A study of the pre-storm environment of tornadic quasi-linear convective systems. In: Conf. on Severe Local Storms Abstracts. Vol. 22, pp. 3A–5.

Goodman, S.J., Blakeslee, R.J., Koshak, W.J., Mach, D., Bailey, J., Buechler, D., Carey, L., Schultz, C., Bateman, M., McCaul, Jr., E., et al., 2013. The GOES-R geostationary lightning mapper (GLM). Atmos. Res. 125, 34–49.

Grams, J.S., Thompson, R.L., Snively, D.V., Prentice, J.A., Hodges, G.M., Reames, L.J., 2012. A climatology and comparison of parameters for significant Tornado events in the United States. Weather Forecasting 27 (1), 106–123. http://dx.doi.org/10.1175/WAF-D-11-00008.1.

Groenemeijer, P., Kühne, T., 2014. A climatology of tornadoes in Europe: Results from the European severe weather database. Mon. Weather Rev. 142 (12), 4775–4790.

Guo, L., Wang, K., Bluestein, H.B., 2016. Variability of tornado occurrence over the continental United States since 1950. J. Geophys. Res.: Atmos. 121 (12), 6943–6953.

Guyer, J.L., Dean, A.R., 2010. Tornadoes within weak cape environments across the continental united states.

Hanstrum, B.N., Mills, G.A., Watson, A., Monteverdi, J.P., Doswell, C.A., 2002. The cool-season tornadoes of California and southern Australia. Weather. Forecast. 17 (4), 705–722. http://dx.doi.org/10.1175/1520-0434(2002)017<3C0705:TCSTOC>3E2.0.CO;2.

Hersbach, H., Bell, B., Berrisford, P., Hirahara, S., Horányi, A., Muñoz-Sabater, J., Nicolas, J., Peubey, C., Radu, R., Schepers, D., et al., 2020. The ERA5 global reanalysis. Q. J. R. Meteorol. Soc. 146 (730), 1999–2049. http://dx.doi.org/10.1002/qj.3803.

Hoskins, B.J., Valdes, P.J., 1990. On the existence of storm-tracks. J. Atmos. Sci. 47 (15), 1854–1864.

Hua, Z., Anderson-Frey, A., 2023. How are tornadic supercell soundings significantly different from nearby baseline environments? Geophys. Res. Lett. 50 (8), e2022GL102580.

Inoue, H.Y., Kusunoki, K., Kato, W., Suzuki, H., Imai, T., Takemi, T., Bessho, K., Nakazato, M., Hoshino, S., Mashiko, W., et al., 2011. Finescale Doppler radar observation of a tornado and low-level misocyclones within a winter storm in the Japan sea coastal region. Mon. Weather Rev. 139 (2), 351–369.

Jacques-Coper, M., Garreaud, R.D., 2015. Characterization of the 1970s climate shift in South America. Int. J. Climatol. 35 (8), 2164–2179.

Jiménez-Cavero, C.M., 2025. Tornado en el litoral de huelva. Tiempo Clima 5 (88), http://dx.doi.org/10.30859/ameTyCn88p36.

Johns, R.H., Davies, J.M., Leftwich, P.W., 1993. Some wind and instability parameters associated with strong and violent tornadoes: 2. Variations in the combinations of wind and instability parameters. Geophys. Monogr. Ser. 79, 583–590.

Juliá, C., Rahn, D.A., Rutllant, J.A., 2012. Assessing the influence of the MJO on strong precipitation events in subtropical, semi-arid north-central Chile (30 S). J. Clim. 25 (20), 7003–7013.

Kiefer, L.A., Chavas, D.R., Gore, M.J., Dawson, II, D.T., 2026. The climatological relationship between United States tornadoes and extratropical cyclones. Mon. Weather Rev. e250049.

King, J.R., Parker, M.D., Sherburn, K.D., Lackmann, G.M., 2017. Rapid evolution of cool season, low-CAPE severe thunderstorm environments. Weather. Forecast. 32 (2), 763–779.

Kis, A.K., Straka, J.M., 2010. Nocturnal tornado climatology. Weather. Forecast. 25 (2), 545–561.

Kottek, M., Grieser, J., Beck, C., Rudolf, B., Rubel, F., 2006. World map of the Köppen-Geiger climate classification updated. Meteorol. Z. 15 (3), 259–263.

Kounkou, R., Mills, G., Timbal, B., 2009. A reanalysis climatology of cool-season tornado environments over southern Australia. Int. J. Clim.: A J. R. Meteorol. Soc. 29 (14), 2079–2090.

Lacroix, M., Couto, F.T., Gunnell, Y., 2026a. Dual drivers of European severe weather: How the NAO and low-frequency climate variability modulate the seasonal transition from shear-to CAPE-dominated tornadogenesis. Weather. Clim. Extrem. 100920.

Lacroix, M., Couto, F.T., Gunnell, Y., 2026b. Intense autumn and winter tornadoes in a region of low convective available potential energy: Insights from western continental Europe (1940–2022). Atmos. Res. 109169.

Legaard, K.R., Thomas, A.C., 2006. Spatial patterns in seasonal and interannual variability of chlorophyll and sea surface temperature in the California current. J. Geophys. Res.: Ocean. 111 (C6).

León-Cruz, J.F., 2025. Tornadic environments in Mexico. Atmos. Res. 315, 107916. http://dx.doi.org/10.1016/j.atmosres.2025.107916.

Lipari, G., Monteverdi, J., 2000. Convective and shear parameters associated with northern and central california tornadoes during the period 1990–94. In: Preprints, 20th Conf. on Severe Local Storms, Orlando, FL, Amer. Meteor. Soc. pp. 518–521.

Lopes, M.M., Nascimento, E.L., 2024. Atmospheric environments associated with tornadoes in southern Brazil and neighboring areas as compared to other modes of convective hazards: MM Lopes, EL Nascimento. Clim. Dyn. 62 (5), 3641–3667.

Lovell, L.T., Parker, M.D., 2022. Simulated QLCS vortices in a high-shear, low-CAPE environment. Weather. Forecast. 37 (6), 989–1012.

Maas, M., Supinie, T., Berrington, A., Emmerson, S., Aidala, A., Gavan, M., 2024. The tornado archive: Compiling and visualizing a worldwide, digitized tornado database. Bull. Am. Meteorol. Soc. 105, E1137–E1152.

Maher, N., Kay, J.E., Capotondi, A., 2022. Modulation of ENSO teleconnections over North America by the Pacific decadal oscillation. Environ. Res. Lett. 17 (11), 114005.

Mantua, N.J., Hare, S.R., 2002. The Pacific decadal oscillation. J. Ocean. 58 (1), 35–44.

Marín, J.C., Barrett, B.S., Pozo, D., 2021. The tornadoes of 30–31 may 2019 in south-central Chile: Sensitivity to topography and SST. Atmos. Res. 249, 105301. http://dx.doi.org/10.1016/j.atmosres.2020.105301.

Marín, J.C., Gutiérrez, F., Gensini, V.A., Barrett, B.S., Pozo, D., Jacques-Coper, M., Veloso-Aguila, D., 2024. Climatological aspects of notable tornado events in Chile. Mon. Weather Rev. 152 (8), 1803–1819.

Markowski, P.M., Richardson, Y.P., 2009. Tornadogenesis: Our current understanding, forecasting considerations, and questions to guide future research. Atmos. Res. 93 (1–3), 3–10.

Markowski, P., Richardson, Y., 2011. Mesoscale Meteorology in Midlatitudes. John Wiley & Sons.

Markowski, P., Richardson, Y., 2013. How to make a tornado. Weatherwise 66 (4), 12–19.

Martinez, J., Junquas, C., Bozkurt, D., Viale, M., Fita, L., Trachte, K., Campozano, L., Arias, P.A., Boisier, J.P., Condom, T., et al., 2024. Recent progress in atmospheric modeling over the Andes–part I: Review of atmospheric processes. Front. Earth Sci. 12, 1427783.

Mass, C., 2021. The Weather of the Pacific Northwest. University of Washington Press.

McAvoy, B., Jones, W., Moore, P., 2000. Investigation of an unusual storm structure associated with weak to occasionally strong tornadoes over the eastern United States. In: Preprints, 20th Conf. on Severe Local Storms, Orlando, FL, Amer. Meteor. Soc. Vol. 182, p. 185.

McCaul, Jr., E.W., 1993. Observations and simulations of hurricane-spawned tornadic storms. Geophys. Monogr. Ser. 79, 119–142.

McCaul, Jr., E.W., Weisman, M.L., 2001. The sensitivity of simulated supercell structure and intensity to variations in the shapes of environmental buoyancy and shear profiles. Mon. Weather Rev. 129 (4), 664–687.

Miller, G.R., Mogil, H.M., 2011. Oregon's weather and climate: Wet, dry, hot, and cold. Weatherwise 64 (6), 12–19.

Mo, K.C., Higgins, R.W., 1998. Tropical influences on California precipitation. J. Clim. 11 (3), 412–430.

Montana, J., Morales, C., Nicora, M.G., Ardila, J., Schurch, R., Aranguren, D., 2021. Lightning activity over Chilean territory. J. Geophys. Res.: Atmos. 126 (16), e2021JD034580.

Montecinos, A., Aceituno, P., 2003. Seasonality of the ENSO-related rainfall variability in central Chile and associated circulation anomalies. J. Clim. 16 (2), 281–296.

Monteverdi, J.P., Blier, W., Stumpf, G., Pi, W., Anderson, K., 2001. First WSR-88D documentation of an anticyclonic supercell with anticyclonic tornadoes: The Sunnyvale–Los Altos, California, tornadoes of 4 may 1998. Mon. Weather Rev. 129 (11), 2805–2814.

Monteverdi, J.P., Braun, S.A., Trimble, T.C., 1988. Funnel clouds in the San Joaquin Valley, California. Mon. Weather Rev. 116 (3), 782–789.

Monteverdi, J.P., Doswell, C.A., Lipari, G.S., 2003. Shear parameter thresholds for forecasting tornadic thunderstorms in northern and central California. Weather. Forecast. 18 (2), 357–370.

Monteverdi, J.P., Quadros, J., 1994. Convective and rotational parameters associated with three tornado episodes in northern and central California. Weather. Forecast. 9 (3), 285–300. http://dx.doi.org/10.1175/1520-0434(1994)009<3C0285:CARPAW>3E2.0.CO;2.

Moore, T.W., 2018. Annual and seasonal tornado trends in the contiguous United States and its regions. Int. J. Climatol. 38 (3), 1582–1594.

NOAA, 2022. Significant hail parameter (SHiP). https://www.spc.noaa.gov/exper/soundings/help/ship.html. (Accessed 8 August 2026).

Nouri, N., Devineni, N., Were, V., Khanbilvardi, R., 2021. Explaining the trends and variability in the United States tornado records using climate teleconnections and shifts in observational practices. Sci. Rep. 11 (1), 1741.

Parker, M.D., 2012. Impacts of lapse rates on low-level rotation in idealized storms. J. Atmos. Sci. 69 (2), 538–559.

Patricola, C.M., O'Brien, J.P., Risser, M.D., Rhoades, A.M., O'Brien, T.A., Ullrich, P.A., Stone, D.A., Collins, W.D., 2020. Maximizing ENSO as a source of western US hydroclimate predictability. Clim. Dyn. 54 (1), 351–372.

Pilguj, N., Taszarek, M., Allen, J.T., Hoogewind, K.A., 2022. Are trends in convective parameters over the United States and Europe consistent between reanalyses and observations? J. Clim. 35 (12), 3605–3626. http://dx.doi.org/10.1175/JCLI-D-21-0135.1.

Pilorz, W., Laskowski, I., Surowiecki, A., Taszarek, M., Łupikasza, E., 2024. Comparing ERA5 convective environments associated with hailstorms in Poland between 1948–1955 and 2015–2022. Atmos. Res. 301, 107286. http://dx.doi.org/10.1016/j.atmosres.2024.107286.

Poręba, S., Taszarek, M., Ustrnul, Z., 2022. Diurnal and seasonal variability of ERA5 convective parameters in relation to lightning flash rates in Poland. Weather. Forecast. 37 (8), 1447–1470.

Pozo, D., Marín, J.C., Gutiérrez, F., 2023. Cloud properties of cold fronts affecting central Chile: Low and high freezing level storms. Earth Space Sci. 10 (8), e2022EA002591.

Púčik, T., Groenemeijer, P., Rỳva, D., Kolář, M., 2015. Proximity soundings of severe and nonsevere thunderstorms in central Europe. Mon. Weather Rev. 143 (12), 4805–4821.

Rakov, V.A., Uman, M.A., 2003. Lightning: Physics and Effects. Cambridge University Press.

Rasmussen, E.N., 2003. Refined supercell and tornado forecast parameters. Weather. Forecast. 18 (3), 530–535.

Rasmussen, E.N., Blanchard, D.O., 1998. A baseline climatology of sounding-derived supercell and tornado forecast parameters. Weather. Forecast. 13 (4), 1148–1164.

Reboita, M.S., Ambrizzi, T., Rocha, R.P.d., 2009. Relationship between the southern annular mode and southern hemisphere atmospheric systems. Rev. Bras. Meteorol. 24, 48–55.

Rojas, Y., Minder, J.R., Campbell, L.S., Massmann, A., Garreaud, R., 2021. Assessment of GPM IMERG satellite precipitation estimation and its dependence on microphysical rain regimes over the mountains of south-central Chile. Atmos. Res. 253, 105454.

Romps, D.M., 2021. Accurate expressions for the dewpoint and frost point derived from the Rankine–Kirchhoff approximations. J. Atmos. Sci. 78 (7), 2113–2116. http://dx.doi.org/10.1175/JAS-D-20-0301.1.

Rotunno, R., Klemp, J.B., 1982. The influence of the shear-induced pressure gradient on thunderstorm motion. Mon. Weather Rev. 110 (2), 136–151.

Sabol, A.T., Nowotarski, C.J., 2025. Evolution of southern plains supercells and tornadoes through the early evening transition. J. Oper. Meteorol. 13 (1).

Salio, P., Bechis, H., Ribeiro, B.Z., de Lima Nascimento, E., Galligani, V., Garcia, F., Alvarenga, L., Alvarezs Imaz, M.d.l.M., Baissac, D.M., Barle, M.F., et al., 2024. Toward a south American high-impact weather reports database. Bull. Am. Meteorol. Soc. 105 (7), E1204–E1217. http://dx.doi.org/10.1175/BAMS-D-23-0063.1.

Scaff, L., Rutllant, J.A., Rahn, D., Gascoin, S., Rondanelli, R., 2017. Meteorological interpretation of orographic precipitation gradients along an Andes west slope basin at 30 S (Elqui Valley, Chile). J. Hydrometeorol. 18 (3), 713–727.

Schenkman, A.D., Xue, M., Hu, M., 2014. Tornadogenesis in a high-resolution simulation of the 8 may 2003 Oklahoma City supercell. J. Atmos. Sci. 71 (1), 130–154.

Schmit, T.J., Griffith, P., Gunshor, M.M., Daniels, J.M., Goodman, S.J., Lebair, W.J., 2017. A closer look at the ABI on the GOES-R series. Bull. Am. Meteorol. Soc. 98 (4), 681–698.

Schultz, C.J., Petersen, W.A., Carey, L.D., 2009. Preliminary development and evaluation of lightning jump algorithms for the real-time detection of severe weather. J. Appl. Meteorol. Clim. 48 (12), 2543–2563.

Schumacher, R.S., Hence, D.A., Nesbitt, S.W., Trapp, R.J., Kosiba, K.A., Wurman, J., Salio, P., Rugna, M., Varble, A.C., Kelly, N.R., 2021. Convective-storm environments in subtropical South America from high-frequency soundings during RELAMPAGO-CACTI. Mon. Weather Rev. 149 (5), 1439–1458. http://dx.doi.org/10.1175/MWR-D-20-0293.1.

Sherburn, K.D., Parker, M.D., 2014. Climatology and ingredients of significant severe convection in high-shear, low-CAPE environments. Weather. Forecast. 29 (4), 854–877. http://dx.doi.org/10.1175/WAF-D-13-00041.1.

Sherburn, K.D., Parker, M.D., Davenport, C.E., Sirico, R.A., Blaes, J.L., Black, B., McLamb, S.E., Mugrage, M.C., Rackliffe, R.M., 2019. Partnering research, education, and operations via a cool season severe weather soundings program. Bull. Am. Meteorol. Soc. 100 (2), 307–320.

Sherburn, K.D., Parker, M.D., King, J.R., Lackmann, G.M., 2016. Composite environments of severe and nonsevere high-shear, low-CAPE convective events. Weather. Forecast. 31 (6), 1899–1927.

Shikhov, A., Chernokulsky, A., Sprygin, A., Yarinich, Y.I., 2022. Estimation of convective atmospheric instability during squalls, Tornadoes, and large hail events from satellite observations and ERA5 reanalysis data. Atmos. Ocean. Opt. 35 (6), 793–801. http://dx.doi.org/10.1134/S1024856022060227.

Strader, S.M., Gensini, V.A., Ashley, W.S., Wagner, A.N., 2024. Changes in tornado risk and societal vulnerability leading to greater tornado impact potential. NPJ Nat. Hazards 1 (1), 20. http://dx.doi.org/10.1038/s44304-024-00019-6.

Swain, D.L., Lebassi-Habtezion, B., Diffenbaugh, N.S., 2015. Evaluation of nonhydrostatic simulations of northeast Pacific atmospheric rivers and comparison to in situ observations. Mon. Weather Rev. 143 (9), 3556–3569.

Székely, G.J., Rizzo, M.L., et al., 2013. Energy statistics: A class of statistics based on distances. J. Statist. Plann. Inference 143 (8), 1249–1272.

Taszarek, M., Allen, J.T., Marchio, M., Brooks, H.E., 2021a. Global climatology and trends in convective environments from ERA5 and rawinsonde data. NPJ Clim. Atmos. Sci. 4 (1), 35. http://dx.doi.org/10.1038/s41612-021-00190-x.

Taszarek, M., Allen, J.T., Púčik, T., Hoogewind, K.A., Brooks, H.E., 2020. Severe convective storms across Europe and the United States. Part II: ERA5 environments associated with lightning, large hail, severe wind, and tornadoes. J. Clim. 33 (23), 10263–10286.

Taszarek, M., Pilguj, N., Allen, J.T., Gensini, V., Brooks, H.E., Szuster, P., 2021b. Comparison of convective parameters derived from ERA5 and MERRA-2 with rawinsonde data over Europe and North America. J. Clim. 34 (8), 3211–3237. http://dx.doi.org/10.1175/JCLI-D-20-0484.1.

Thompson, R.L., Edwards, R., Hart, J.A., Elmore, K.L., Markowski, P., 2003. Close proximity soundings within supercell environments obtained from the rapid update cycle. Weather. Forecast. 18 (6), 1243–1261. http://dx.doi.org/10.1175/1520-0434(2003)018<3C1243:CPSWSE>3E2.0.CO;2.

Thompson, R.L., Edwards, R., Mead, C.M., Center, S.P., 2004a. An update to the supercell composite and significant tornado parameters. In: Preprints, 22nd Conf. on Severe Local Storms, Hyannis, MA, Amer. Meteor. Soc., P8.1. [Available Online at https://Ams.Confex.Com/Ams/Pdfpapers/82100.Pdf].

Thompson, R.L., Mead, C., Edwards, R., 2004b. Effective bulk shear in supercell thunderstorm environments. In: Preprints, 22 nd Conf. on Severe Local Storms, Hyannis, MA, Amer. Meteor. Soc.,(this Volume).

Thompson, R.L., Mead, C.M., Edwards, R., 2007. Effective storm-relative helicity and bulk shear in supercell thunderstorm environments. Weather. Forecast. 22 (1), 102–115.

Thompson, R.L., Smith, B.T., Grams, J.S., Dean, A.R., Broyles, C., 2012. Convective modes for significant severe thunderstorms in the contiguous United States. Part II: Supercell and QLCS tornado environments. Weather. Forecast. 27 (5), 1136–1154.

Tippett, M.K., Malloy, K., Lee, S.H., 2024. Modulation of us tornado activity by year-round north American weather regimes. Mon. Weather Rev. 152 (9), 2189–2202.

Tuckman, P., Emanuel, K., 2024. Origins of extreme CAPE around the world. J. Geophys. Res.: Atmos. 129 (22), e2024JD041833.

Tyrrell, J., 2007. Winter tornadoes in Ireland: The case of the Athlone tornado of 12 january 2004. Atmos. Res. 83 (2–4), 242–253.

Valenzuela, R.A., Garreaud, R.D., 2019. Extreme daily rainfall in central-southern Chile and its relationship with low-level horizontal water vapor fluxes. J. Hydrometeorol. 20 (9), 1829–1850.

Van Den Broeke, M.S., Schultz, D.M., Johns, R.H., Evans, J.S., Hales, J.E., 2005. Cloud-to-ground lightning production in strongly forced, low-instability convective lines associated with damaging wind. Weather. Forecast. 20 (4), 517–530.

Van Wagtendonk, J.W., Cayan, D.R., 2008. Temporal and spatial distribution of lightning strikes in California in relation to large-scale weather patterns. Fire Ecol. 4 (1), 34–56.

Veloso-Aguila, D., Rasmussen, K.L., Maloney, E.D., 2024. Tornadoes in Southeast South America: Mesoscale to planetary-scale environments. Mon. Weather Rev. 152 (1), 295–318. http://dx.doi.org/10.1175/MWR-D-22-0248.1.

Viale, M., Houze, Jr., R.A., Rasmussen, K.L., 2013. Upstream orographic enhancement of a narrow cold-frontal rainband approaching the Andes. Mon. Weather Rev. 141 (5), 1708–1730.

Viale, M., Norte, F.A., 2009. Strong cross-barrier flow under stable conditions producing intense winter orographic precipitation: A case study over the subtropical central Andes. Weather. Forecast. 24 (4), 1009–1031.

Viale, M., Valenzuela, R., Garreaud, R.D., Ralph, F.M., 2018. Impacts of atmospheric rivers on precipitation in southern south America. J. Hydrometeorol. 19 (10), 1671–1687.

Vicencio, J., Rondanelli, R., Campos, D., Valenzuela, R., Garreaud, R., Reyes, A., Padilla, R., Abarca, R., Barahona, C., Delgado, R., et al., 2021. The Chilean tornado outbreak of may 2019: Synoptic, mesoscale, and historical contexts. Bull. Am. Meteorol. Soc. 102 (3), E611–E634. http://dx.doi.org/10.1175/BAMS-D-19-0218.1.

Wade, A.R., Parker, M.D., 2021. Dynamics of simulated high-shear, low-CAPE supercells. J. Atmos. Sci. 78 (5), 1389–1410.

Wapler, K., 2017. The life-cycle of hailstorms: Lightning, radar reflectivity and rotation characteristics. Atmos. Res. 193, 60–72.

Wicker, L., Cantrell, L., 1996. The role of vertical buoyancy distributions in miniature supercells. In: Preprints, 18th Conf. on Severe Local Storms, San Francisco, CA, Amer. Meteor. Soc. Vol. 225, p. 229.

Wilks, D.S., 2011. Statistical Methods in the Atmospheric Sciences. Vol. 100, Academic Press.

Williams, E., Mushtak, V., Rosenfeld, D., Goodman, S., Boccippio, D., 2005. Thermodynamic conditions favorable to superlative thunderstorm updraft, mixed phase microphysics and lightning flash rate. Atmos. Res. 76 (1–4), 288–306.

Yu, R., Du, M., Zheng, D., Wang, J., 2025. Analysis of anomalous cloud-to-ground lightning in a Wuhan tornadic supercell on 14 may 2021. Atmos. Res. 320, 108056.

Zhang, J., Ni, X., 2026. Investigating the spatial distribution differences of hail and lightning in North America. Nat. Hazards 122 (5), 205.

Zhang, R., Xue, M., Yu, X., 2025. Environments of tornadic and non-tornadic supercells in China and optimized significant tornado parameter for China region. Q. J. R. Meteorol. Soc. 151 (772), e5027. http://dx.doi.org/10.1002/qj.5027.

Zhou, R., Meng, Z., Bai, L., 2022. Differences in tornado activities and key tornadic environments between China and the United States. Int. J. Climatol. 42 (1), 367–384. http://dx.doi.org/10.1002/joc.7248.